

Article

Buck-Boost/Flyback Hybrid Converter for Solar Power System Applications

Sheng-Yu Tseng * and Jun-Hao Fan

Department of Electrical Engineering, Chang Gung University, Guishan District, Taoyuan City 33302, Taiwan; m0921014@cgu.edu.tw

* Correspondence: sytseng@mail.cgu.edu.tw; Tel.: +886-3-211-8800 (ext. 5706)

Abstract: This paper proposes a hybrid converter to supply power from solar power source to load. Since power is generated by solar power, which depends on the intensity of solar power, the power generated by the solar power does not keep at a constant power. Therefore, the proposed system needs a battery to balance power between solar power and load. When the proposed one uses the battery to balance powers, the proposed circuit requires a charger and discharger. To simplify the proposed converter, a buck-boost converter and flyback converter can be combined to implement the battery charging and discharging functions. With this approach, the proposed converter can be operated with zero-voltage switching (ZVS) at turn-on transition to reduce switching loss of switch when the proposed one is operated in the discharging mode. In addition, the proposed hybrid converter has several merits, which are less component counts, lighter weight, smaller size and higher conversion efficiency. As compared with the conventional counterparts with hard-switching circuit, the proposed one can increase conversion efficiency of 4% and achieve efficiency of 85% under full load condition when the proposed one is operated in the discharging mode. Experimental results which are obtained from a prototype with output voltage of 10 V and maximum output power 20 W have been implemented to verify its feasibility. It is suitable for an electronic sign indicating LED within 200 W, which is used in the night time.



Citation: Tseng, S.-Y.; Fan, J.-H. Buck-Boost/Flyback Hybrid Converter for Solar Power System Applications. *Electronics* **2021**, *10*, 414. <https://doi.org/10.3390/electronics10040414>

Academic Editor:

Sergio Busquets-Monge

Received: 22 December 2020

Accepted: 30 January 2021

Published: 8 February 2021

Publisher's Note: MDPI stays neutral with regard to jurisdictional claims in published maps and institutional affiliations.



Copyright: © 2021 by the authors. Licensee MDPI, Basel, Switzerland. This article is an open access article distributed under the terms and conditions of the Creative Commons Attribution (CC BY) license (<https://creativecommons.org/licenses/by/4.0/>).

Keywords: charger; discharger; ZVS; buck-boost converter; flyback converter; solar power and battery

1. Introduction

Nowadays, due to a drastic increase in the demand for electricity, it leads to rapid and depletion of fossil fuels. In particular, when Taiwan Semiconductor Manufacturing (TSMC) and Google data center were built in Taiwan, electricity demand was increased by 1/3 within 5 years. As a result, the power processor adopts renewable energy sources as its input sources. In the renewable energy sources, such as solar power, wind turbine and fuel cell, they have been widely applied to a switching-mode converter for generating electric power to load [1,2]. They include power generation for grid connection, electric vehicles, water pumps, battery charger and discharger, traffic signals, street-lighting, electronic signs, and so on.

Due to the most recent development of light emitting diodes (LEDs) technology, it possesses many advantages, such as smaller size, longer lifetime, lower maintenance costs and greater strength against breakage [3–6]. Therefore, LEDs have widely used in our daily lives. They are suitable for indoor and outdoor energy-saving lighting applications, such as automotive taillights, thin film transistor liquid crystal display (TFT-LCD) backlight, traffic signals, streetlights, electronic signs [7–10]. In particular, the electronic sign or streetlight is used in the night time. It is suitable for solar power sources to supply power when solar power sources are adopted in the electronic sign or streetlight system. That is, the power system uses a charger to store energy from solar power sources to battery in the daytime, while the one adopts a discharger to release energy from battery to LEDs in the

night time. The proposed power system simultaneously needs a charger and discharger, as shown in Figure 1.

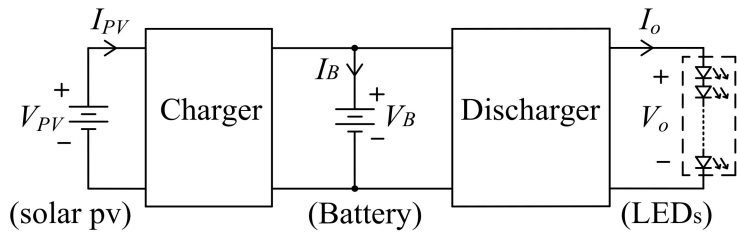


Figure 1. Block diagram of solar power system for electronic signor street-lighting application.

Since the proposed power system adopts PV sources as its input source, the one needs the charger and discharger for electronic sign or streetlight application. The output voltage of solar power source is less than or greater than that of battery (8 V~12 V). Therefore, it simultaneously needs a step-up and step-down converter, such as buck-boost, 'cuk, zeta and sepic converter [11–13]. As compared with 'cuk, zeta and sepic converter, buck-boost converter possesses a simpler circuit topology. It is chosen as the charger for battery system, as shown in Figure 2. Since the flyback converter possesses many merits, which are a simpler circuit topology, wider ranges of voltage ratio between input voltage and output voltage and a lower cost, it can be applied to the solar power system or battery system. Therefore, the proposed power system can adopt buck-boost converter and flyback converter to implement battery charging and discharging functions, simultaneously, as shown in Figure 3.

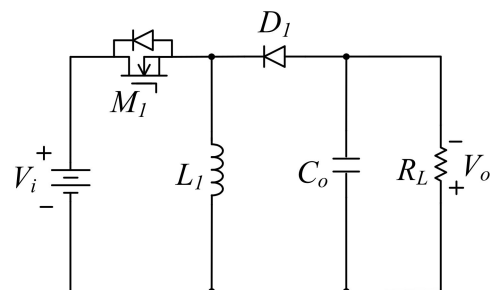


Figure 2. Schematic diagram of buck-boost converter for battery charging applications.

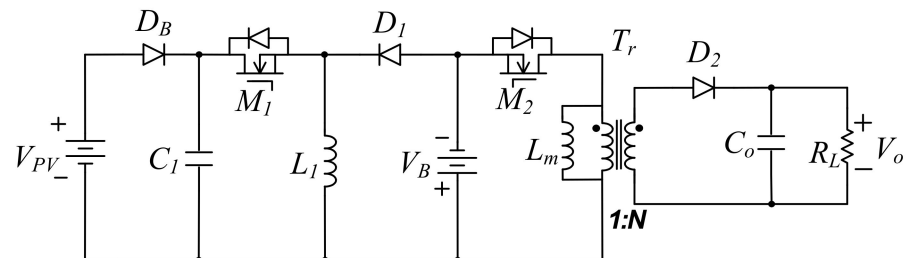


Figure 3. Schematic diagram of buck-boost/flyback hybrid converter for battery charging and discharging applications.

When the proposed power system uses the flyback converter as the discharger, the leakage inductor of transformer will induce a spike voltage across switch. As a result, it will generate an extra switching loss. To avoid this problem, an active clamp circuit can be added into the flyback converter to recover leakage inductor energy [14–17], as shown in Figure 4. In order to simplify circuit topology, switches of the charger and discharger can be respectively integrated, as shown in Figure 5. From Figure 5, the proposed hy-

brid converter can use a less component count to implement the battery charging and discharging functions, simultaneously. Therefore, the proposed power system can reduce cost, weight and size. Furthermore, the proposed one can be operated in ZVS at turn-on transition to increase conversion efficiency. It is suitable for a PV power system.

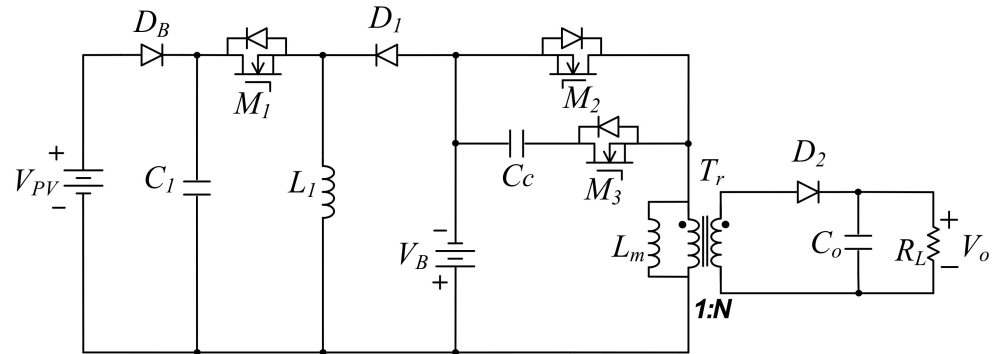


Figure 4. Schematic diagram of buck-boost/flyback converter with active clamp circuit for solar power applications.

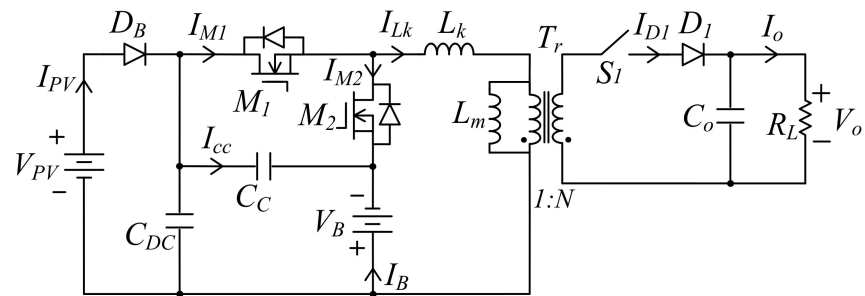


Figure 5. Schematic diagram of the proposed hybrid converter for solar power applications.

2. Derivation of the Proposed Hybrid Converter

The proposed hybrid converter adopts a buck-boost converter as the battery charger and a flyback converter as the battery discharger, as shown in Figure 4. In order to simplify the proposed power system, a bidirectional buck-boost converter is used and an active clamp circuit is introduced into flyback converter to increase conversion efficiency, as shown in Figure 6. From Figure 6, since the battery charger and discharger in the proposed power system are operated in complementary, switch S_1 is added into the proposed one to keep the battery charging and discharging functions. When switch S_1 is regarded as the operational mode switch, switches M_2 and M_3 shown in Figure 6 can be merged as a switch M_2 illustrated in Figure 5, while switches M_1 and M_4 can be merged as a switch M_1 . The inductor L_1 can be also merged with the magnetizing inductor L_m of transformer. With this approach, the proposed power system can use a less component count to achieve the battery charging and discharging functions.

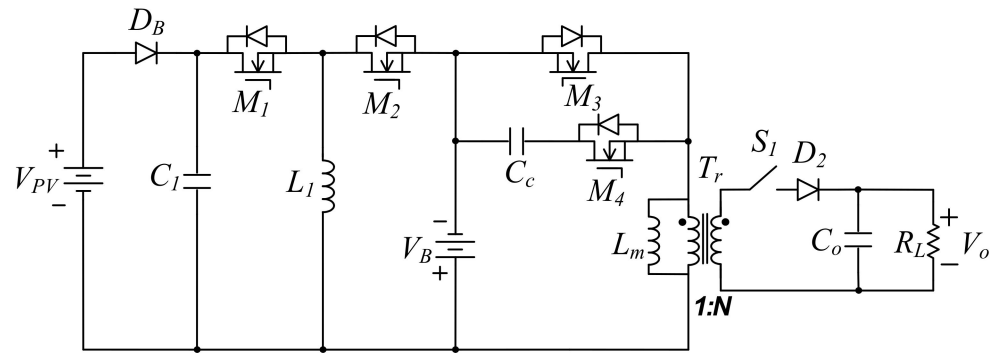
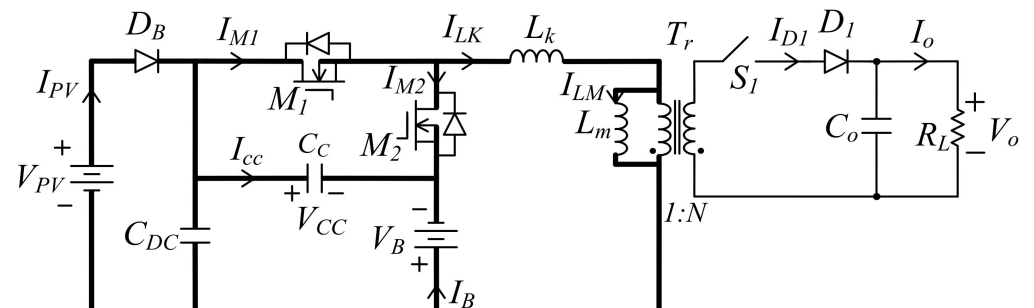
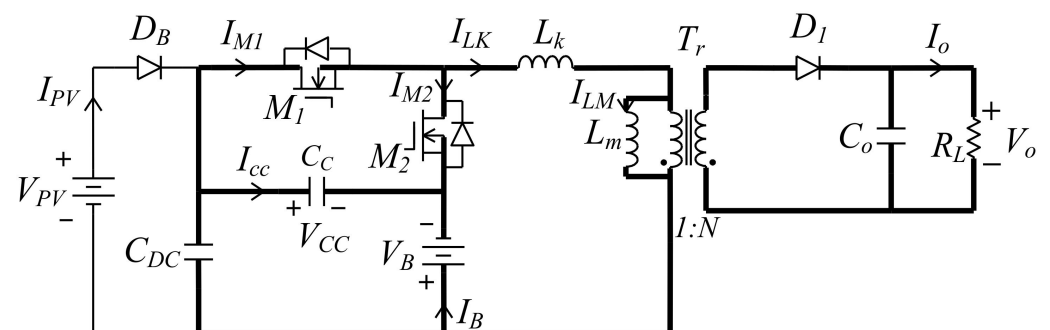


Figure 6. Schematic diagram of the convention bidirectional buck-boost/flyback hybrid converter for solar power applications.

When the proposed power system is operated in the charging mode, switch S_1 is turned off. The equivalent circuit of the proposed one is the same as a buck-boost converter, as shown in Figure 7a. In Figure 7a, the magnetizing inductor of transformer T_r is respected as the inductor of the buck-boost one, where topology of the proposed hybrid converter operated in the charging mode is highlighted with thick line. When the proposed one is operated in discharging mode, switch S_1 is turned on, its equivalent circuit is the same as active clamp flyback converter, as shown in Figure 7b. In Figure 7b, the proposed hybrid one is highlighted with thick line. Therefore, the proposed power system can be respectively operated in different modes by the operational conditions of switch S_1 .



(a)



(b)

Figure 7. Schematic diagram of the proposed hybrid converter operated in (a) the charging mode, and (b) the discharging mode.

3. Operational Principle of the Proposed Power System

The proposed hybrid converter can be divided into two operational modes: the charging mode and the discharging mode. Its equivalent circuit of the different operational modes is shown in Figure 7. Since the proposed hybrid converter can be operated in two different modes, its operational principle for each operational mode is also described in the following, respectively.

The charging mode

When the proposed hybrid converter is operated in the charging mode, its operational modes can be divided into 6 modes. The equivalent circuit of each operational mode and conceptual waveforms are plotted in Figures 8 and 9, respectively. The power flow of each operational mode in the proposed hybrid converter is highlighted with thick line, as shown in Figure 9. In the following, each operational mode is briefly described.

Mode 1 [Figure 9a: $t_0 \leq t < t_1$]: Before t_0 , switch M_1 is in the turn-on state and switch M_2 is in the turn-off state. During this time interval, switch current I_{M1} abruptly increases from 0A to the initial value of inductor L_m operated in continuous condition mode (CCM). When $t = t_0$, switch M_1 is still in the turn-on state, and M_2 is kept in the turn-off state. Since inductance L_m is further greater than L_k , voltage V_{PV} is approximately applied to inductance L_m . During this time interval, inductor L_m is in the stored energy state. Inductor current I_{Lm} linearly increases. The charging current I_B equals 0A.

Mode 2 [Figure 9b: $t_1 \leq t < t_2$]: At $t = t_1$, switch M_1 is turned off and switch M_2 is still in the turn-off state. During this time interval, capacitor voltage V_{CM2} is discharging from $(V_{PV} + V_B)$ to 0V, while V_{CM1} is charged from 0V to $(V_{PV} + V_B)$. Within this mode, switch current I_{M1} abruptly decreases from the maximum value to 0A, and current I_{M2} quickly increases from 0V to the maximum value.

Mode 3 [Figure 9c: $t_2 \leq t < t_3$]: At $t = t_2$, body diode D_{M2} is in the forwardly bias state. Energy stored in magnetizing inductor L_m is released through battery and body diode D_{M2} . Inductor current I_{Lm} linearly reduces. The battery is in the charging state.

Mode 4 [Figure 9d: $t_3 \leq t < t_4$]: At t_3 , switch M_2 is turned on and M_1 is kept in the turn-off state. Since body diode D_{M2} is forwardly biased before $t = t_3$, switch M_2 is operated at ZVS at turn-on transition. Energy stored in magnetizing inductor L_m is still in the released energy state. Current I_{Lm} is equal to charging current I_B , and its value linearly increases.

Mode 5 [Figure 9e: $t_4 \leq t < t_5$]: At $t = t_4$, switch M_2 is turned off, and M_1 is kept at the turn-off state. Since energy stored in inductor current I_{Lm} is released through battery and body diode D_{M2} , switch voltage V_{M1} is kept at 0V. Capacitor voltage V_{CM1} is also kept at $(V_{PV} + V_B)$. Inductor current I_{Lm} linearly reduces.

Mode 6 [Figure 9f: $t_5 \leq t < t_6$]: At $t = t_5$, switch M_1 is turned on, and M_2 is kept in the turn-off state. Due to body diode D_{M2} is in the forwardly bias state before $t = t_5$, switch voltage V_{M1} abruptly varies from $(V_{PV} + V_B)$ to 0V, switch voltage V_{M2} fast changes from 0V to $(V_{PV} + V_B)$. Switch current I_{M1} suddenly increases to the initial value when the proposed converter is operated in CCM. Switch current I_{M2} and battery current I_B simultaneously decreases to 0A. Since this time interval is very short, current I_{M1} is kept at the initial value and current I_{M2} and battery current I_B are sustained at 0A. When $t = t_6$, a new switching cycle will start.

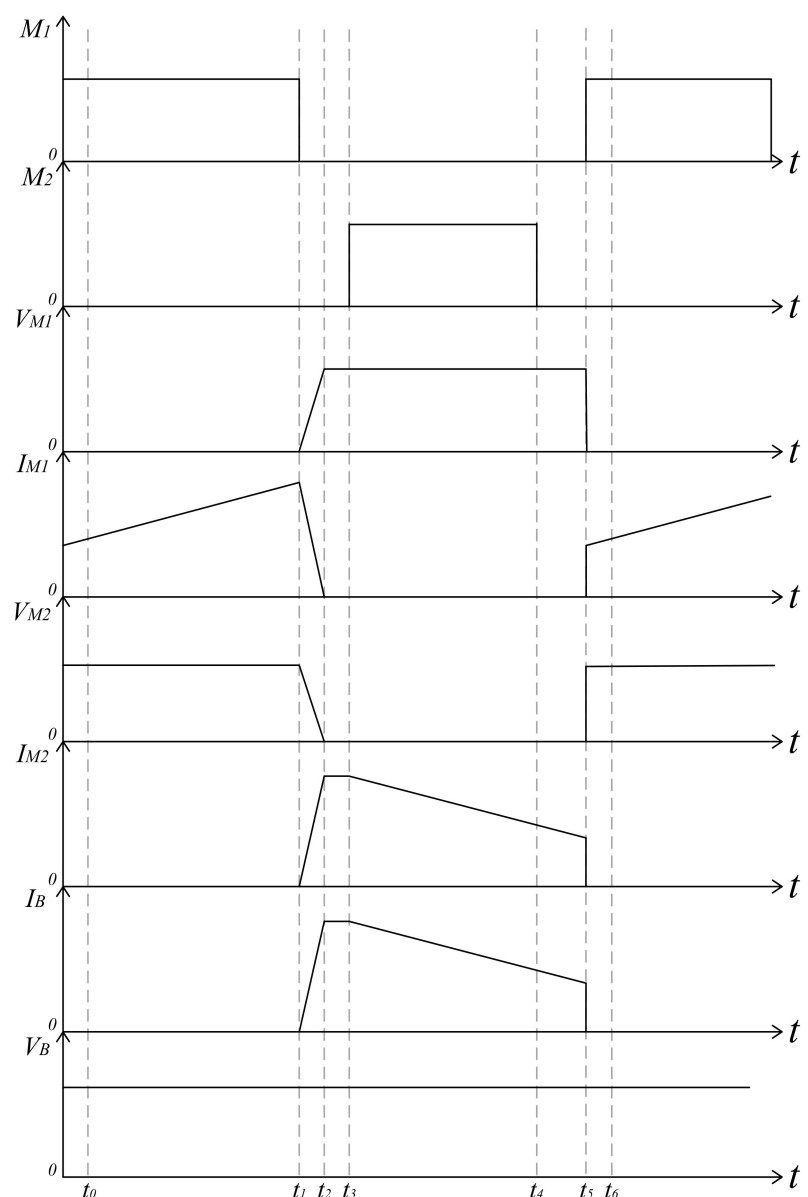
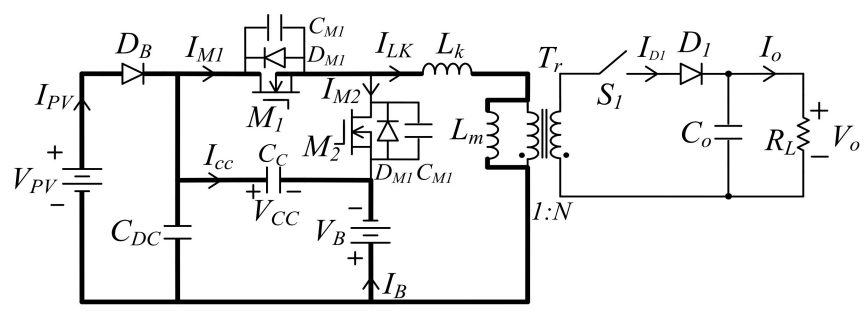
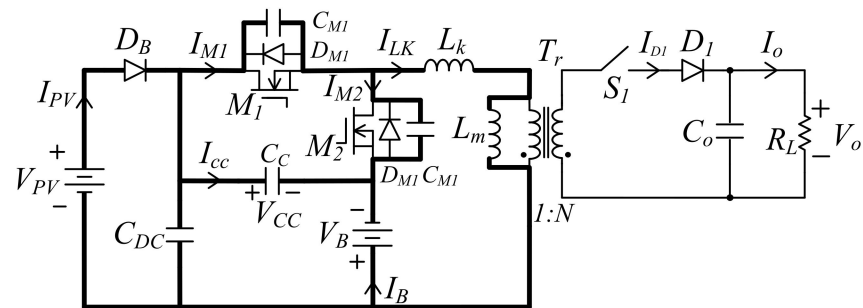


Figure 8. Conceptual waveforms of the propose hybrid converter operated in the charging mode.

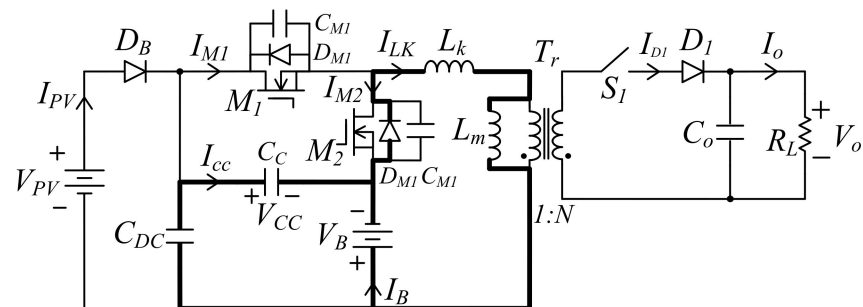


(a)

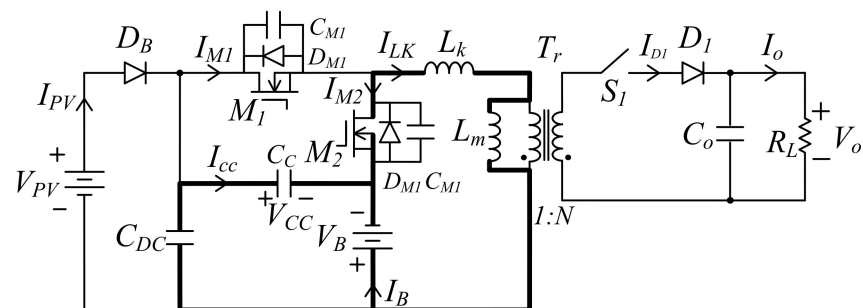
Figure 9. Cont.



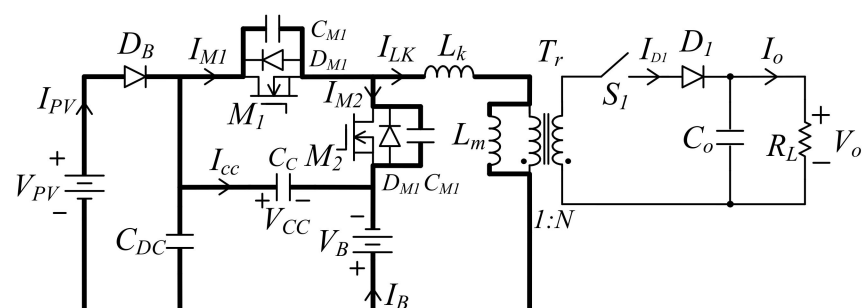
(b)



(c)

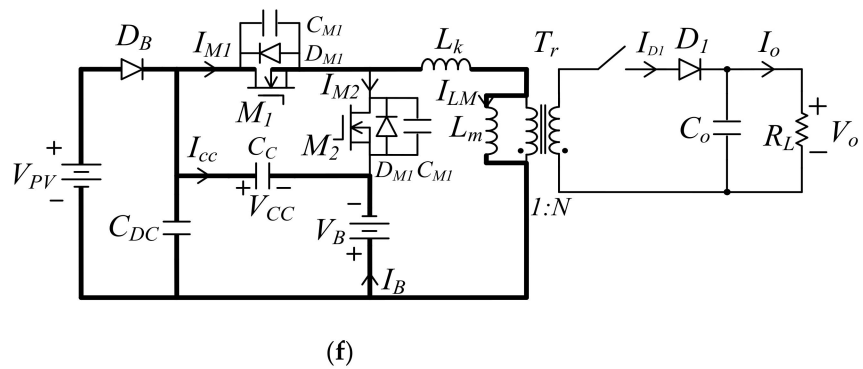


(d)



(e)

Figure 9. Cont.



(f)

Figure 9. Equivalent circuit of the proposed hybrid converter operated in the charging mode over one switching cycle; (a) Mode 1 ($t_0 \leq t < t_1$); (b) Mode 2 ($t_1 \leq t < t_2$); (c) Mode 3 ($t_2 \leq t < t_3$); (d) Mode 4 ($t_3 \leq t < t_4$); (e) Mode 5 ($t_4 \leq t < t_5$); (f) Mode 6 ($t_5 \leq t < t_6$).

The discharging mode

When the proposed hybrid converter is operated in the discharging mode during the night time, PV arrays does not generate power to supply battery. Furthermore, the proposed one with battery is required to supply energy to lighting system. According to the previously requirements, switch S_1 is turned on and PV arrays are not to supply power to load by diode D_B . Its equivalent circuit is implemented by flyback with active clamp circuit, as shown in Figure 7b. When the proposed hybrid converter is formed with the active clamp flyback converter, its operational mode is divided into eight modes. Its key component waveform is illustrated in Figure 10. In addition, equivalent circuit of each operational mode is depicted in Figure 11. In the following, each operational mode is described briefly.

Mode 1 [Figure 11a: $t_0 \leq t < t_1$]: Before t_0 , switch M_2 is in the turn-on state and switch M_1 is in the turn-off state. Switch current I_{M2} fast varies from 0A to the initial value of inductor L_m in the proposed converter operated in CCM. When $t = t_0$, switch M_2 is still in the turn-on state, and M_1 is kept in the turn-off state. Switch current I_{M2} is equal to the initial value of inductor current I_{Lm} . During this time interval, magnetizing inductor L_m is in the stored energy state. Inductor current I_{Lm} linearly increases. Since diode D_1 is reversely biased, load power is supplied by output capacitor C_o .

Mode 2 [Figure 11b: $t_1 \leq t < t_2$]: At t_1 , switch M_2 is turned off and switch M_1 is still in the turn-off state. Since inductor current I_{LK} must be operated in the continuous condition through capacitor C_{M1} and C_{DC} , Capacitor C_{M1} is discharged and its voltage V_{M1} varies from $(V_o/N + V_B)$ to 0V. Within this mode, capacitor C_o supplies power to load. Switch current I_{M2} abruptly decreases to 0A, while current I_{M1} suddenly reduced to the negative maximum value. Capacitor current I_{CC} also varies from 0V to its maximum value.

Mode 3 [Figure 11c: $t_2 \leq t < t_3$]: When $t = t_2$, body diode D_{M1} is forwardly biased and diode D_1 is also in the forwardly bias. Inductor voltage V_{Lm} is clamped at $(-V_o/N)$. During this time interval, leakage inductor L_k and capacitor C_C form a resonant network. Inductor current I_{Lk} varies with the resonant form from the maximum value to the negative maximum value. Energy stored in the magnetizing inductor L_m is released through secondary winding of transformer T_r and diode D_1 to load.

Mode 4 [Figure 11d: $t_3 \leq t < t_4$]: At $t = t_3$, switch M_1 is turned on and M_2 is kept in the turn-off state. Because body diode D_{M1} is in the forwardly bias state before $t = t_3$, switch M_1 is operated with ZVS at turn-on transition. Within this mode, inductor L_k and capacitor C_c connects in series to generate the resonance. Inductor current I_{Lk} is still in the resonant state, and current I_{Lm} linearly reduce to release the energy stored in the magnetizing inductor L_m .

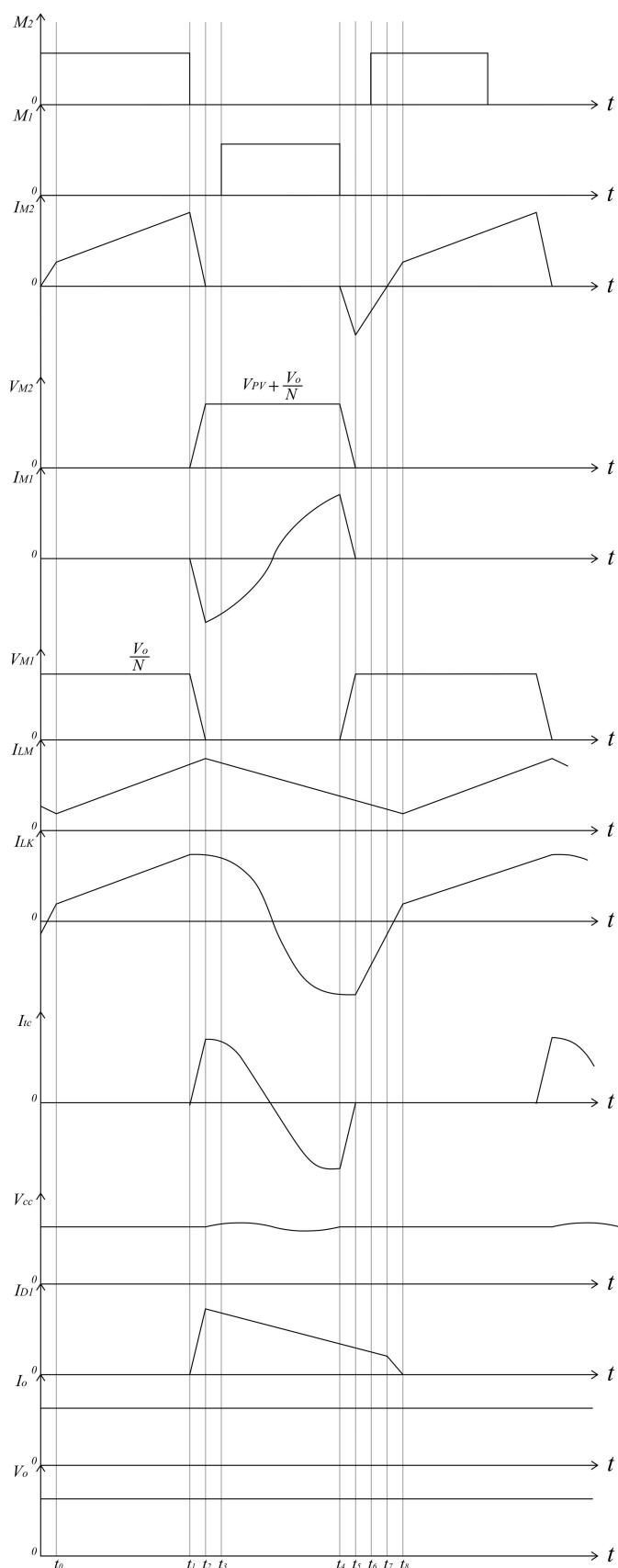
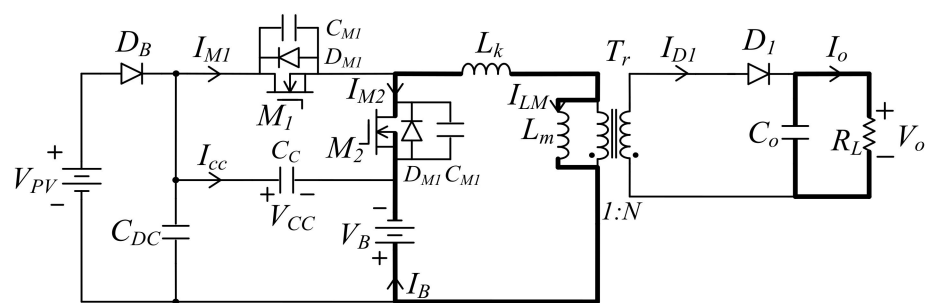
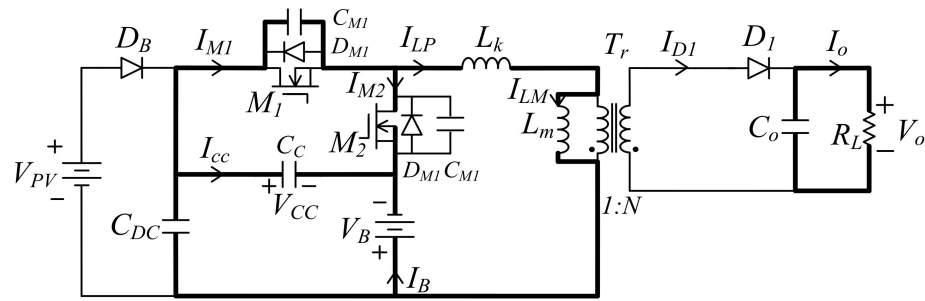


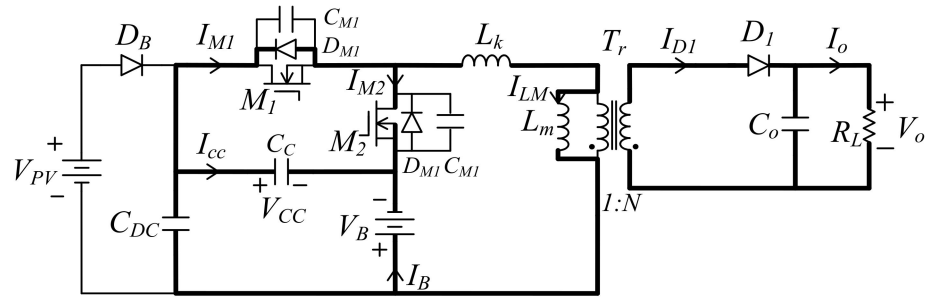
Figure 10. Conceptual waveforms of the propose hybrid converter operated in the discharging mode.



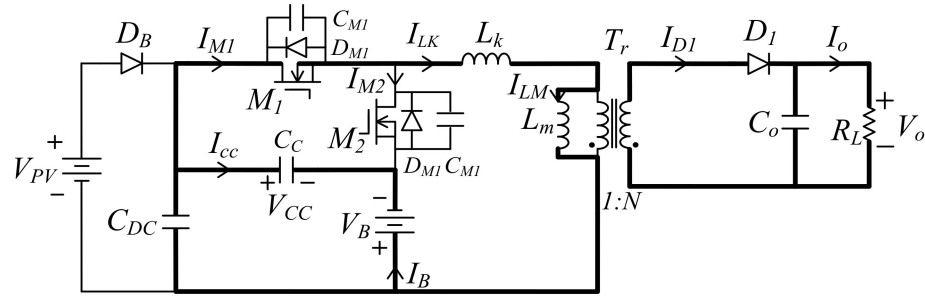
(a)



(b)



(c)



(d)

Figure 11. Cont.

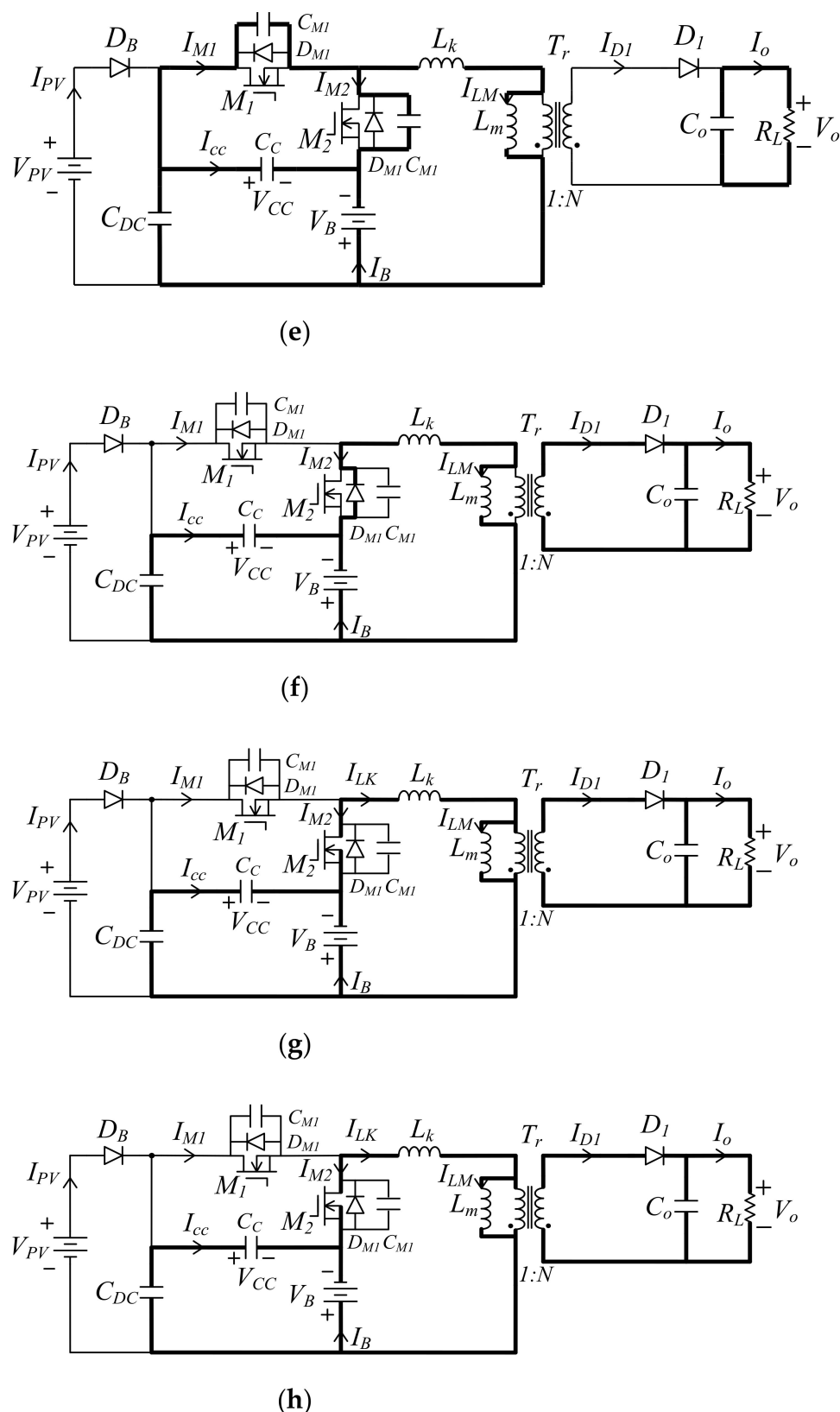


Figure 11. Equivalent circuit of the proposed hybrid converter operated in the discharging mode over one switching cycle. (a) Mode 1 ($t_0 \leq t < t_1$); (b) Mode 2 ($t_1 \leq t < t_2$); (c) Mode 3 ($t_2 \leq t < t_3$); (d) Mode 4 ($t_3 \leq t < t_4$); (e) Mode 5 ($t_4 \leq t < t_5$); (f) Mode 6 ($t_5 \leq t < t_6$); (g) Mode 7 ($t_6 \leq t < t_7$); (h) Mode 8 ($t_7 \leq t < t_8$).

Mode 5 [Figure 11e: $t_4 \leq t < t_5$]: At t_4 , switch M_1 is turned off, and M_2 is kept at the turn-off state. Since capacitor C_{M1} enters the charging state, capacitor voltage V_{M1} varies from 0V to $(V_o/N + V_B)$. Moreover, capacitor voltage V_{M2} works in the discharging state, voltage V_{M2} change from $(V_o/N + V_B)$ to 0V. Within this mode, energy stored in the magnetizing inductor L_m releases through diode D_1 to load. Inductor current I_{Lm} linearly reduces.

Mode 6 [Figure 11f: $t_5 \leq t < t_6$]: When $t = t_5$, capacitor voltage V_{M1} is clamped at $(V_o/N + V_B)$, while voltage V_{M2} is kept at 0V. At the moment, body diode D_{M2} is forwardly biased. During this time interval, inductor current I_{LK} equals to current I_{M2} . Their values abruptly varies from the negative maximum value to 0V. The magnetizing inductor L_m is still in the discharging energy state, and its current I_{Lm} linearly decreases.

Mode 7 [Figure 11g: $t_6 \leq t < t_7$]: When $t = t_6$, switch M_2 is turned on, and switch M_1 is still kept in the turn-off state. Since body diode D_{M2} is in the forwardly bias state before t_6 , switch M_2 is operated with ZVS at turn-on transition. During this time interval, current I_{LK} ($=I_{M2}$) changes from a negative value to 0V. The magnetizing inductor L_m is still in the released energy state through diode D_1 to load. Its current I_{Lm} linearly reduces.

Mode 8 [Figure 11h: $t_7 \leq t < t_8$]: At t_7 , switch M_2 is in the turn-on state and M_1 is in the turn-off state. During this time interval, inductor current I_{LK} varies from 0A to the initial value. The magnetizing inductor L_m is kept in the released energy state. Therefore, current I_{Lm} linearly decreases. When operational mode is at the end of mode 8, one new switching cycle will start.

4. Design of the Proposed Hybrid Converter

The proposed hybrid converter includes a charger and discharger. When the proposed one is operated as the charger, its equivalent circuit is the same as buck-boost converter. Moreover, its equivalent circuit is formed with an active clamp flyback converter for the discharger. Since the proposed one is composed with charger and discharger, its design must satisfy requirements of each converter. In the following, each converter is briefly analyzed.

A. Charger: Buck-boost converter

Since the battery charger is adopted with buck-boost converter, its key parameters include duty ratio D_{11} and inductor L_m . Therefore, duty ratio D_{11} and inductor L_m are derived in the following.

A.1 Duty ratio D_{11}

In the light day, the proposed hybrid converter is regarded as the charger. The power flows from PV arrays to battery. During switching cycle, battery voltage V_B is almost kept at a constant value. For maximum power point tracking (MPPT) of solar power, the proposed one can regulate the charging current I_B to implement MPPT. The maximum duty ratio $D_{11(max)}$ can be determined under the minimum output voltage $V_{PV(min)}$ of solar power and maximum battery voltage $V_{B(max)}$. Its relationship is expressed as

$$V_{PV(min)}D_{11(max)}T_s + (-V_{B(max)})\left(1 - D_{11(max)}\right)T_s = 0, \quad (1)$$

where T_s represents the period of the proposed hybrid converter. From (1), $D_{11(max)}$ can be derived by

$$D_{11(max)} = \frac{V_{B(max)}}{V_{PV(min)} + V_{B(max)}}. \quad (2)$$

In addition, maximum transfer ratio $M_{11(max)}$ can be obtained as

$$M_{11(max)} = \frac{D_{11(max)}}{1 - D_{11(max)}}. \quad (3)$$

According to the above equations, when type of battery is selected, the maximum charging current $I_{B(max)}$ can be denoted. Moreover, the charging current I_B can be changed

from its maximum charging current $I_{B(max)}$ to 0A by regulating duty ratio D_{11} of switch M_1 . The charging current I_B is determined by MPPT of solar power.

A.2 Inductor L_m

In order to obtain the inductance L_m , the boundary inductance L_{mB} , which is the inductor value of the proposed converter operated in the boundary of CCM and discontinuous condition mode (DCM). Its conceptual waveforms are illustrated in Figure 12. The average charging current $I_{B(av)}$ can be determined as

$$I_{B(av)} = \frac{\Delta I_{Lm(max)}(1 - D_{11})}{2}, \quad (4)$$

where $\Delta I_{Lm(max)}$ represents a maximum current variation of inductor L_m . In (4), $\Delta I_{Lm(max)}$ can be expressed by

$$\Delta I_{Lm(max)} = \frac{V_{PV}D_{11}T_s}{L_{mB}} = \frac{V_B(1 - D_{11})T_s}{L_{mB}} \quad (5)$$

where V_{PV} is the output voltage of solar power and V_B represents the battery voltage. According to (4) and (5), the charging current $I_{B(av)}$ can be obtained as

$$I_{B(av)} = \frac{(1 - D_{11})^2 V_B T_s}{2 L_{mB}}. \quad (6)$$

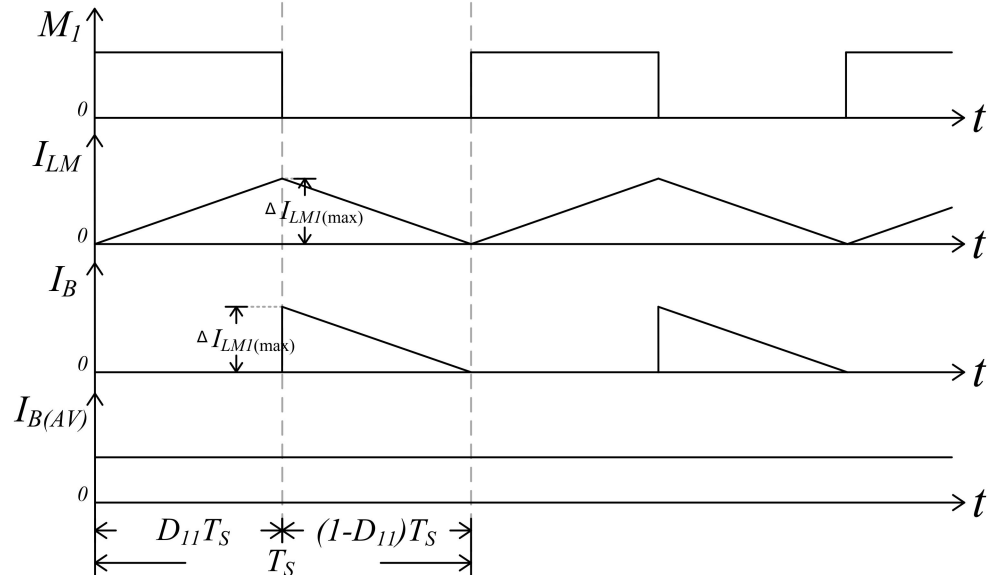


Figure 12. Conceptual waveforms of inductor current I_{Lm} and charging current I_B in the charger.

Since the maximum charging current $I_{B(av)max}$ occurs at the maximum battery voltage $V_{B(max)}$ and the minimum PV voltage $V_{PV(min)}$, the maximum charging current $I_{B(av)max}$ can be rewritten with

$$I_{B(av)max} = \frac{(1 - D_{11(min)})^2 V_{B(max)} T_s}{2 L_{mB}}, \quad (7)$$

where $D_{11(min)}$ represents duty ratio from $V_{B(max)}$ to $V_{PV(max)}$. Since the charger is always operated in CCM, $I_{B(av)max}$ can be expressed by $K_1 I_{B(max)}$, where K_1 varies from 0 to 1 and

$I_{B(max)}$ is the maximum charging current. In general, K_1 is set at 0.1~0.3. From (7), it can be seen that inductor L_{m1} can be expressed as

$$L_{m1} = \frac{(1 - D_{11(min)})^2 V_{B(max)} T_s}{2K_1 I_{B(max)}}. \quad (8)$$

A.3. selection of switches

Figure 7a shows the schematic diagram of the proposed hybrid converter operated in the charging mode. In order to determine voltage and V_{PV} is at the maximum value and battery voltage V_B is at maximum value, voltage ratings of components in the proposed one can be determined. Maximum voltage stresses of M_1 and M_2 can be determined by

$$V_{M1(max)} = V_{M2(max)} = V_{PV(max)} + V_{B(max)}. \quad (9)$$

In addition, voltage stress of switch S_1 obtained as

$$V_{S1(max)} = N V_{B(max)} \quad (10)$$

When input voltage V_{PV} is at minimum value and battery voltage V_B is at maximum value, the maximum *rms* current $I_{M(rms)}$ of switch M_1 can be illustrated by

$$I_{M1(rms)} = \frac{I_{B(max)}}{1 - D_{11(max)}} \sqrt{D_{11(max)} [1 + \frac{r^2}{12}]}, \quad (11)$$

where r is defined by ($\frac{\Delta I_{Lm}}{I_{B(max)}}$). The maximum *rms* current $I_{M2(rms)}$ of switch M_2 can be derived as

$$I_{M2(rms)} = I_{B(max)} \sqrt{\frac{[1 + \frac{r^2}{12}]}{1 - D_{11(max)}}}. \quad (12)$$

Moreover, the maximum *rms* current $I_{LK(rms)}$ of inductor L_M can be obtained as

$$I_{LK(rms)} = \frac{I_{B(max)}}{1 - D_{11(max)}} \sqrt{1 + \frac{r^2}{12}}. \quad (13)$$

Discharger: Active clamp flyback converter

When the proposed boost converter is operated in the discharging mode, its equivalent circuit is composed by flyback converter with the active clamp circuit. For design of active clamp flyback converter, the important parameters include duty ratio D_{12} , transformer T_r , active clamp capacitor C_C and output capacitor C_o . In the following, their designs are analyzed briefly.

B.1. Duty ratio D_{12}

When the proposed hybrid converter uses flyback converter with the active clamp circuit to achieve soft-switching features, the active clamp circuit does not affect transfer ratio M_{12} of the proposed flyback converter. That is, transfer ratio M_{12} is the same as the conventional one. According to volt-second balance of inductor L_m , the following equation can be obtained by

$$V_B D_{12} T_s + \left(-\frac{V_o}{N} \right) (1 - D_{12}) T_s = 0, \quad (14)$$

where $N (=N_2/N_1)$ is the turns ratio of transformer T_r . From (9), it can be found that transfer ratio M_{12} can be represented as

$$M_{12} = \frac{ND_{12}}{(1 - D_{12})}. \quad (15)$$

When the output to input voltage transfer ratio M_{12} is determined, duty ratio D_{12} can be obtained by

$$D_{12} = \frac{V_o}{NV_B + V_o}. \quad (16)$$

In the (11), when N , V_o and V_B are specified, duty ratio D_{12} can be determined.

B.2. Transformer T_r

In order to Design transformer T_r , turns ratio N and the magnetizing inductor L_m are important parameters. Since output current I_o can be determined by inductance L_m and turns ratio N , their conceptual waveforms is shown in Figure 13. From Figure 13, it can be found that the average diode current $I_{D1(av)}$ is represented by

$$I_{D1(av)} = \frac{\Delta I_{Lm2(max)}(1 - D_{12})}{2N}, \quad (17)$$

where $\Delta I_{Lm2(max)}$ is the variation value of inductor current I_{Lm2} . According to operational principle of the proposed hybrid converter, inductor current $\Delta I_{Lm2(max)}$ is obtained with

$$\Delta I_{Lm2(max)} = \frac{V_{B(max)}D_{12}T_s}{L_{MB2}}, \quad (18)$$

where L_{MB2} is the magnetizing inductance of transformer T_r where the proposed hybrid converter is operated in the boundary of DCM and CCM.

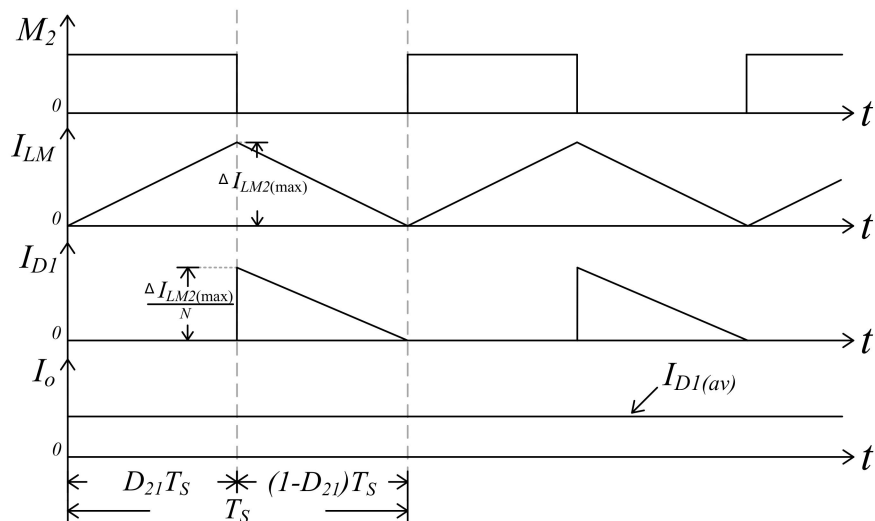


Figure 13. Conceptual waveforms of inductor current I_{Lm} and output current I_o in the discharger.

Since the proposed one adopts the active clamp circuit to achieve soft-switching features, its magnetizing inductor L_{m2} is always operated in CCM. Therefore, the proposed one is designed in CCM under light load condition. The average current $I_{D1(av)}$ is equal to $K_2 I_{o(max)}$, where K_2 range from 0 to 1 and $I_{o(max)}$ represents the maximum output current. According to (12) and (13), the magnetizing inductor L_{m2} can be determined by

$$L_{m2} = \frac{V_{B(max)}D_{12}(1 - D_{12})T_s}{2NK_2 I_{o(max)}}. \quad (19)$$

Since the magnetizing inductor L_m is separately operated in the charging and discharging modes, their inductances are derived with different values (L_{m1} and L_{m2}), respectively. In order to design a proper inductance L_m , it is selected with the maximum value between L_{m1} and L_{m2} .

In (10) and (11), when voltage V_B and V_o are specified, turns ratio N is inversely proportional to duty ratio D_{12} . Since a large duty ratio D_{12} corresponds to a smaller turns ratio N of transformer T_r . That is, lower current stresses are imposed on switches M_1 and M_2 . However, in order to tolerate variations of load, battery voltage and component value, it is better to select an operating ranges as $D = 0.35\sim0.4$. When duty ratio D_{12} is specified, turns ratio N can be determined.

B.3. Active clamp capacitor C_C

When the proposed hybrid converter adopts the active clamp to achieve soft-switching features, the active clamp capacitor C_C can be used to recover energy trapped in leakage inductor L_k and help switch to achieve ZVS features. In order to obtain a wider range of soft-switching features, a half of resonant period is equal to or greater than turn-off time of switch M_2 when capacitor C_C and leakage inductor L_k are formed as the resonant network. Therefore, capacitor C_C must satisfy the following inequality:

$$\pi\sqrt{L_k C_C} \geq (1 - D_{12})T_s. \quad (20)$$

According to (15), capacitor C_C can be expressed by

$$C_C \geq \frac{(1 - D_{12})^2 T_s^2}{\pi^2 L_k}. \quad (21)$$

In (10), once leakage inductor L_k is specified, capacitor C_C can be determined.

B.4. Output Capacitor C_o

Since output capacitor C_o is used to reduce ripple of output voltage V_o , its value must be large enough. The ripple voltage ΔV_o across output capacitor C_o is expressed as follows:

$$\Delta V_o = \frac{I_{o(max)} D_{12} T_s}{C_o}, \quad (22)$$

where $I_{o(max)}$ is the maximum output current. Therefore, output capacitor C_o can be determined by

$$C_o = \frac{I_{o(max)} D_{12} T_s}{\Delta V_o}. \quad (23)$$

When the maximum output current $I_{o(max)}$, duty ratio D_{12} , switching cycle T_s and output ripple voltage ΔV_o are specified, output capacitor C_o can be determined by (18).

B.4. Selection of switches and diode

Figure 7a shows the schematic diagram of the proposed hybrid converter operated in the discharging mode. When battery voltage V_B is under a maximum value situation, voltage rating of components can be determined. Maximum voltage stresses of switch M_1 and M_2 can be obtained as

$$V_{M1(max)} = V_{M2(max)} = V_{B(max)} + \frac{V_o}{N}. \quad (24)$$

Maximum voltage stress $V_{D1(max)}$ of diode D_1 can be expressed by

$$V_{D1(max)} = N V_{B(max)} + V_o. \quad (25)$$

When the minimum battery voltage $V_{B(min)}$ and output maximum current $I_{o(max)}$, the maximum rms current $I_{M2(rms)}$ can be derived as

$$I_{M2(rms)} = \frac{N I_{o(max)}}{1 - D_{12(max)}} \sqrt{D_{12(max)} [1 + \frac{r^2}{12}]} \quad (26)$$

The maximum *rms* current $I_{LM2(rms)}$ is expressed by

$$I_{LM2(rms)} = \frac{N I_{o(max)}}{1 - D_{12(max)}} \sqrt{1 + \frac{r^2}{12}}. \quad (27)$$

Moreover, the maximum *rms* current $I_{S1(rms)}$ ($= I_{D1(rms)}$) is indicated by

$$I_{S1(rms)} = I_{D1(rms)} = I_{o(max)} \sqrt{\frac{[1 + \frac{r^2}{12}]}{(1 - D_{12(max)})}}. \quad (28)$$

Since switch M_2 is turned off, inductor L_K and capacitor C_c form a resonant network. A half resonant period of the resonant network is equal to $(1 - D_{12}) T_s$. The current waveform of switch M_1 varies with cosine wave manner. According to the *rms* calculation method for the cosine wave, the maximum *rms* current $I_{M1(rms)}$ can be obtained by

$$I_{M1(rms)} = I_{PK} \sqrt{\frac{1 - D_{12(max)}}{2}}, \quad (29)$$

where $D_{12(max)}$ is cut the minimum battery voltage $V_{B(min)}$ and I_{PK} expresses the maximum current of inductor L_{M2} . When the proposed hybrid converter is operated in the heavy load condition, current I_{PK} is approximately equal to $[N I_{o(max)} / (1 - D_{12(max)}) + \frac{1}{2} \Delta I_{Lm2}]$.

B.5. Power losses analysis

Since the proposed hybrid converter is operated in the charging mode, the proposed one is operated with hard-switching manner. Its power loss analysis is the same as the conventional buck converter.

The power loss analysis is neglected in this paper. When the proposed one is operated in the discharging mode, the active clamp capacitor C_c can be used to recover the energy strapped in leakage inductor L_k to increase conversion efficiency of the proposed one. Therefore, the power loss analysis is described for the proposed one operated in the discharging mode. When the proposed one is operated in the discharging mode, power loss includes losses of switches, diode and core. In the following, power loss analysis is derived.

(1). Losses of switches

The losses of switches include switching loss and conduction loss. Figure 14 shows the conceptual waveforms of switching losses for switches M_1 and M_2 . Since switches M_1 and M_2 is operated with ZVS at turn-on transition, their switching loss is only induced at turn-off transition of switches. Therefore, switching losses P_{soff} of switches M_1 and M_2 can be expressed by

$$P_{soff} = \frac{1}{2T_s} V_{M1(max)} (t_{off} I_{DP}), \quad (30)$$

where I_{DP} is equal to $[N I_{o(max)} / (1 - D_{12(max)}) + \frac{1}{2} \Delta I_{Lm2}]$. The conduction loss of switch M_1 (or M_2) can be derived as

$$P_{CD} = I_{M(rms)}^2 R_{DS(on)}, \quad (31)$$

where $I_{M(rms)}$ is the *rms* current of each switch and $R_{DS(on)}$ represses a resistance of switch during turn-on state.

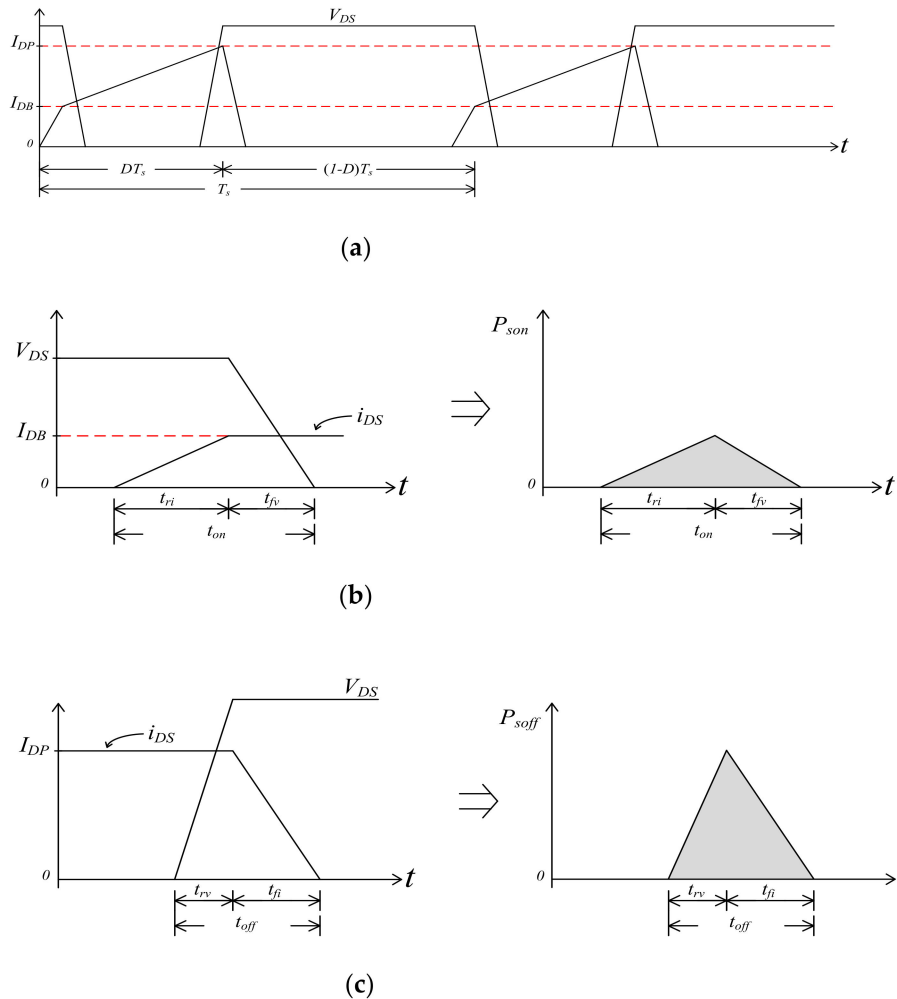


Figure 14. Conceptual waveforms of switching loss during switch turn-on and turn-off transitions (a) during one switching cycle, (b) during turn-on transition (c) during turn-off transition.

(2). Loss of diode

The loss of diode D_1 is generated by the forward voltage V_F when diode D_1 is in the forward biased state. The loss P_{D1} can be derived by

$$P_{D1} = I_{D1(rms)}^2 V_F. \quad (32)$$

(3). Loss of core

The loss of core includes core loss and copper loss. The core loss of transformer T_r is determined by the maximum flux density B_m and core loss curve of core. The maximum flux density B_m can be determined by

$$B_m = \frac{\mu_0 \mu_r N \left(\frac{N I_{o(\max)}}{1 - D_{12(\max)}} + \frac{\Delta I_{Lm2}}{2} \right)}{(l_e + \mu_r l_g)}, \quad (33)$$

where N is the turns of primary winding and l_e expresses the effective magnetic path length, l_g indicates air gap length and μ_r permeability. When B_m is determined, the core loss coefficient C_p can be obtained through core loss curve of core. The core loss P_{CL} is determined as

$$P_{CL} = C_p V_e, \quad (34)$$

where V_e is the effective core volume of core. Moreover, copper loss P_{CPL} can be derived by

$$P_{CPL} = I_{Lm2(rms)}^2 R_{dc1} l_{m1} + I_{D1(rms)}^2 R_{dc2} l_{m2}, \quad (35)$$

where R_{dc1} is the resistance coefficient of wire gauge of primary winding, l_{m1} represses the total length of turns of primary winding, R_{dc2} is the resistance coefficient of wire gauge of secondary winding and l_{m2} indicates the total length of turns of secondary winding.

A. Block diagram of control method of the proposed hybrid converter

In order to control the proposed hybrid converter, a microcontroller and pulse-width modulation integrated circuit (PWM IC) are adopted in the proposed systems, as shown in Figure 15. In Figure 15, the microcontroller is used to implement maximum power point tracking (MPPT) of solar power, manages battery charging, controls battery charging current and perform battery protection. Moreover, the PWM IC is adopted to regulate output voltage V_o . For MPPT, this paper uses the perturb-and-observe method to execute the MPPT of solar power. In order to match the MPPT of solar power, charger adopts constant current (CC) method to implement battery charging.

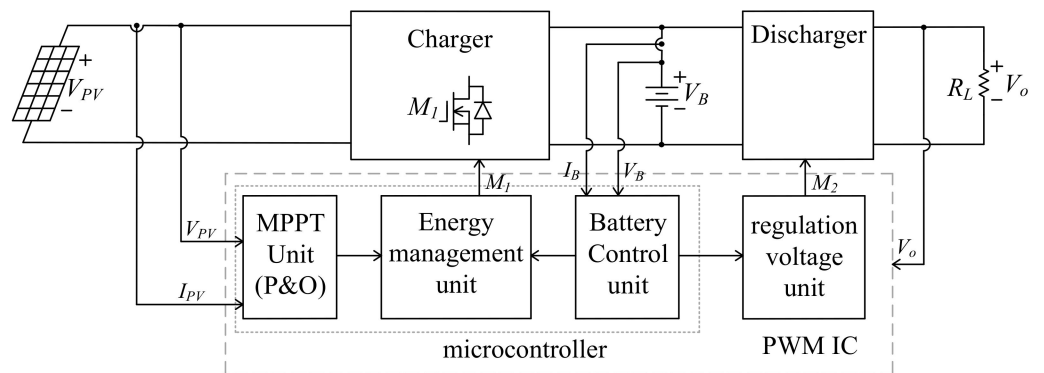


Figure 15. Block diagram of the proposed hybrid converter for solar power system applications.

B. Performances comparison between the proposed hybrid converter and the conventional counterpart converter

In general, key components of switching power supply include the switch, diode, magnetic device, capacitor, printed circuit board (PCB), control IC, driving circuit, filter and resistor, and so on. According to the technical report of the Industrial Economics and Knowledge Center (IEK) in Taiwan, cost of each component in switching power supply is illustrated in Table 1. From Table 1, it can be found that switch, capacitor, magnetic device, diode and driving circuit possess higher cost ratio in the switching power supply. Table 2 lists the component counts comparison between the proposed hybrid converter and the conventional counterpart converter. Since the conventional counterpart converter shown in Figure 4 includes three switches, two magnetic devices, two diodes and two sets of driving circuits, the proposed hybrid converter can reduce component usage and increase an extra switch S_1 usage. When the proposed one reduces one switch usage, it can obtain a cost reduction of 6.7%. In addition, the reduction magnetic device, diode and driving circuit usage of the proposed one can acquire a cost reduction of 8%, 5% and 6%, respectively. In order to reduce component counts, the proposed one increases a cost of 3~6.7%. From Table 2, it can be found that the proposed one can reduce cost of 19~22.7%.

Table 1. Total cost analysis of switching power supply (data from Industrial Economics and Knowledge Center (IEK) in Taiwan).

Component	Cost Ratio = (Cost of Each Item/Total Cost)
switch	20%
capacitor	18%
Magnetic device	16%
diode	10%
PCB	6%
filter	8%
Driving circuit	12%
resistor	5%
Control IC	3%
others	2%

Table 2. Component count comparison between the proposed hybrid converter and the conventional counterpart converter.

Component	The Conventional Hybrid Buck-Boost/Flyback Hybrid Converter (Figure 4)	The Proposed Hybrid Buck-Boost/Flyback Hybrid Converter (Figure 5)	Cost Ratio decrease for the Proposed Hybrid Converter
switch	3 pcs	2 pcs	6.7%
Magnetic device	2 pcs	1 pc	8%
diode	2 pcs	1 pc	5%
capacitor	3 pcs	3 pcs	0%
Driving circuit	2 sets	1 sets	6%
Extra device	0 pc	1 pc	-3~−6.7%

5. Experimental Results

The proposed hybrid converter used solar power as its input source. Specifications of solar power are listed in Table 3. The following specifications were implemented.

Table 3. Specification of the solar power supplied by solar power manufacturer.

Parameter	Values
Maximum power (P_{max})	30 W
Maximum power voltage ($P_{pv(max)}$)	17.5 V
Maximum power current ($I_{pv(max)}$)	1.84 A
Open circuit voltage (V_{oc})	20.9 V
Short circuit current (I_{sc})	1.94 A

A. Charger: Buck-boost converter

- Input voltage V_{PV} : DC 17.5 V~20.6 V (solar power),
- Switching frequency f_{s1} : 50 kHz,
- Output voltage V_B : DC 8 V~12 V (lithium battery:3.2 Ah), and
- Maximum charging current $I_{B(max)}$: 3.2 Ah

B. Discharger: flyback converter

- Input voltage V_B : DC 8 V~12 V (lithium battery:3.2 Ah),
- Switching frequency f_{s2} : 50 kHz,
- Output voltage V_o : DC 10 V, and

- Maximum output current $I_{o(max)}$: 2 A.

According to the previously specifications and design of the proposed hybrid converter, inductor L_m , turns ratio N and active clamp capacitor C_C could be determined. Table 4 illustrates parameters of components of the proposed hybrid converter. According to operational conditions of the proposed one, current and voltage stresses could be determined. From Table 4, it can be obtained that the magnetizing inductor L_m equaled 660 μH and turns ratio N was equal to 2. When transformer T_r was wound with the magnetizing inductor L_m of 660 μH , leakage inductor L_k was measured and its value was 12.5 μH . Therefore, the active capacitor C_C was calculated and its value was 1.62 μF . Capacitor C_C is adopted with 1.5 μF . In addition, current and voltage stresses of the proposed hybrid converter and the conventional counterpart converter are listed in Table 5. From Table 5, it can be found that although component stress of the proposed hybrid converter was higher than that of the conventional counterpart converter, it could use fewer component counters to achieve the charging and discharging functions. The switch S_1 could adopt lower current and voltage stresses to change the charging mode or discharging mode of the proposed one. Furthermore, the components of power stage in the proposed hybrid converter were determined as follows:

- Switches M_1, M_2 : AoW2918,
- Diode D_1 : STPS10L60D,
- Switches S_1 : AoW2918,
- Transformer T_r : EE-33 core, and
- Output capacitor C_o : 47 $\mu\text{F}/25 \text{ V}$.

Figure 16 shows the photo of the proposed hybrid prototype converter. The hardware dimension of the proposed hybrid converter was about $100 \times 60 \text{ mm}^2$. The circuit layout safety distance was set at 5 mm around outside of each component. According to the requirement of safety distance of each component, circuit layout area comparison between the proposed hybrid converter and the conventional counterpart converter is listed in Table 6. When switch M_1 was adopted with AoW2918, its package was TO220. According to dimension of TO220 package, component dimension was $10 \times 5 \text{ mm}^2$. In order to consider safety distance between two components, circuit layout dimension was considered with $20 \times 15 \text{ mm}^2$. Although a component with a heat sink could increase its power processing capacity, its circuit layout dimension was increased. The heat sink dimension for TO220 package was $15 \times 10 \text{ mm}^2$. Therefore, switch with heat sink needed $25 \times 20 \text{ mm}^2$ for switch layout dimension. According to the above requirement to layout the proposed hybrid converter and the conventional counterpart converter, their circuit layout area is respectively calculated in the Table 6. From Table 6, it can be found that the proposed hybrid converter needed a circuit layout area of 6000 mm^2 , while the conventional counterpart converter needed that of 9000 mm^2 . Therefore, the proposed one could reduce circuit layout area by 3000 mm^2 . The power density of the proposed one could increase about 1.5 times.

The proposed hybrid converter used solar power to charge the battery with CC. The MPPT and battery charging with CC must be implemented. When solar power was used as input voltage source, the proposed hybrid converter adopted the perturb-and-observe method to implement MPPT. Measured voltage V_{PV} , current I_{PV} , and power P_{PV} waveforms of solar power is shown in Figure 17. Figure 17a illustrates those waveforms under $P_{PV(max)} = 15 \text{ W}$, while Figure 17b plots those waveforms under $P_{PV(max)} = 30 \text{ W}$. From Figure 17, it can be obtained that tracking time T of solar power was about 200 ms. Figure 18 shows measured gate voltage M_1 of switch M_1 and charging current I_B . Since capacitor C_C connected with inductor L_m in series, they formed a resonant network through battery or capacitor C_{DC} during switch M_1 turn-on or turn-off interval, respectively. The measured charging current I_B varied with a resonant waveform. Figure 18a shows those waveforms under the average charging current $I_{B(av)} = 0.7 \text{ A}$. Moreover, Figure 18b illustrates those waveforms under $I_{B(av)} = 3 \text{ A}$.

Table 4. Parameters of components in the proposed hybrid converter.

Operational Mode	Symbol	Design Value	Practical Value (v)	Conditions	
	Parameter	Equation	Value		
The charging mode	Switch M_1	$V_{M1(max)}$	(9)	33 V	$V_{B(max)} = 12 \text{ V}$
		$I_{M1(rms)}$	(11)	6.20 A	$V_{PV(max)} = 20.6 \text{ V}$
		$I_{M1(pk)}$		8.07 A	$D_{11(max)} = 0.6$
	Switch M_2	$V_{M2(max)}$	(9)	33 V	$D_{11(min)} = 0.368$
		$I_{M2(rms)}$	(12)	5.06 A	$\Delta I_{LM} = 0.64 \text{ A}, r = 0.2$
		$I_{M2(pk)}$		8.07 A	
	Switch S_1	$V_{S1(max)}$	(10)	24 V	$V_{B(max)} = 12 \text{ V}$
		$I_{S1(rms)}$		0 A	$N = 2$
		$I_{S1(pk)}$		0 A	$V_{B(max)} = 12 \text{ V}$
The discharging mode	Inductor L_{m1}	L_{m1}	(8)	150 μH	$\Delta I_{Lmp} = 0.145 \text{ A}$
		$I_{LK(rms)}$	(13)	8.01 A	$r_p = 0.045$
	Switch M_1	$V_{M1(max)}$	(24)	17 V	$I_{LK(rms)} = 8 \text{ A}$
		$I_{M1(rms)}$	(29)	3.92 A	$D_{11(min)} = 0.368, D_{11(max)} = 0.6$
		$I_{M1(pk)}$		7.07 A	$K = 0.1, T_s = 20 \mu\text{s}, V_{B(max)} = 12 \text{ V}, I_{B(max)} = 3.2 \text{ A}$
	Switch M_2	$V_{M2(max)}$	(24)	17 V	$\Delta I_{LM} = 0.64 \text{ A}, r = 0.2$
		$I_{M2(rms)}$	(26)	1.05 A	
		$I_{M2(pk)}$		7.07 A	
	Switch S_1	$V_{S1(max)}$		0 V	$V_{B(max)} = 12 \text{ V}, V_{B(min)} = 8 \text{ V}$
		$I_{S1(rms)}$	(28)	2.56 A	$D_{12(min)} = 0.294, D_{12(max)} = 0.385$
		$I_{S1(pk)}$		3.54 A	$N = 2, V_o = 10 \text{ V}, r = 0.2845$
Capacitor C_c	Transformer T_r	L_{m2}	(19)	62 μA	$I_{o(max)} = 2 \text{ A}$
		$I_{Lm(rms)}$	(27)	6.53 A	
	Diodes	C_c	(21)	1.62 μF	$V_{B(max)} = 12 \text{ V}, D_{12} = 0.294$
				1.5 μF	$K_2 = 0.1, T_s = 20 \mu\text{s}, N = 2$
					$I_{o(max)} = 2 \text{ A}$
					$\Delta I_{Lm2} = 1.138 \text{ A}, r = 0.2845$
					$L_k = 12.5 \mu\text{H}, D_{12(min)} = 0.294$
					$T_s = 20 \mu\text{s}$

Table 5. Current and voltage stresses of components between the proposed hybrid converter and the counterpart converter.

Component	The counterpart Converter Shown in Figure 4			The Proposed Hybrid Converter Shown in Figure 5		
	Symbol	Voltage Stress	Current Stress (rms)	Symbol	Voltage Stress	Current Stress (rms)
switches	M_1	33 V	6.20 A	M_1	33 V	6.20 A
	M_2	17 V	4.04 A	M_2	33 V	5.06 A
	M_3	17 V	3.63 A	S_1	24 V	2.55 A
Diodes	D_1	33 V	5.06 A	D_1	34 V	2.55 A
	D_2	34 V	2.55 A			

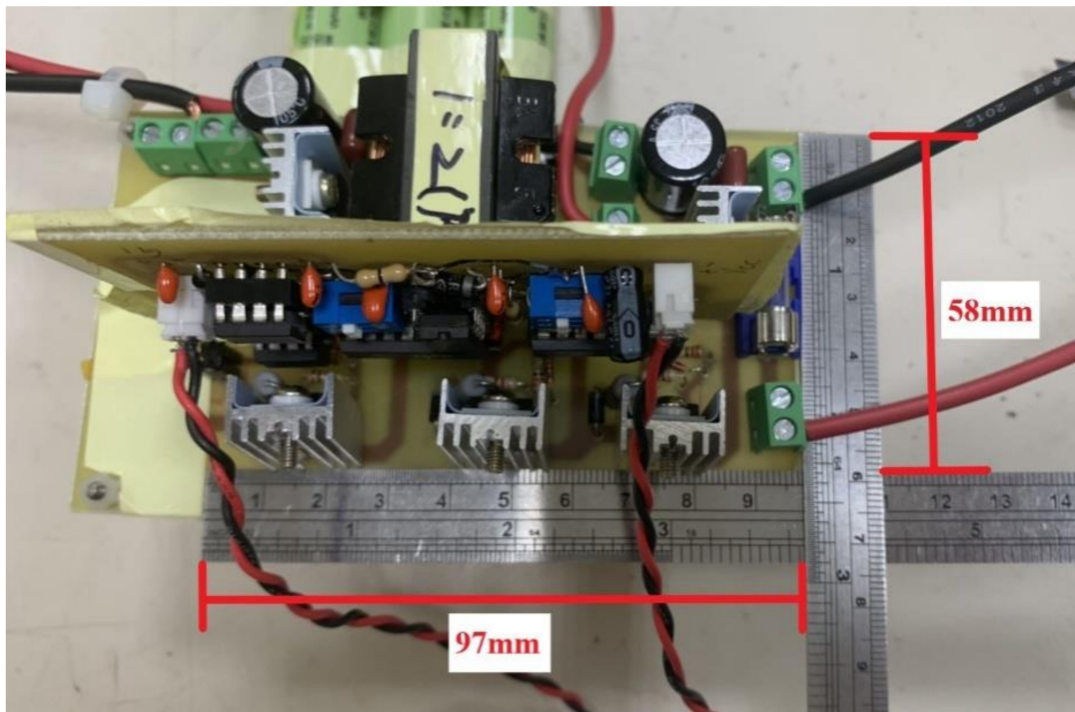
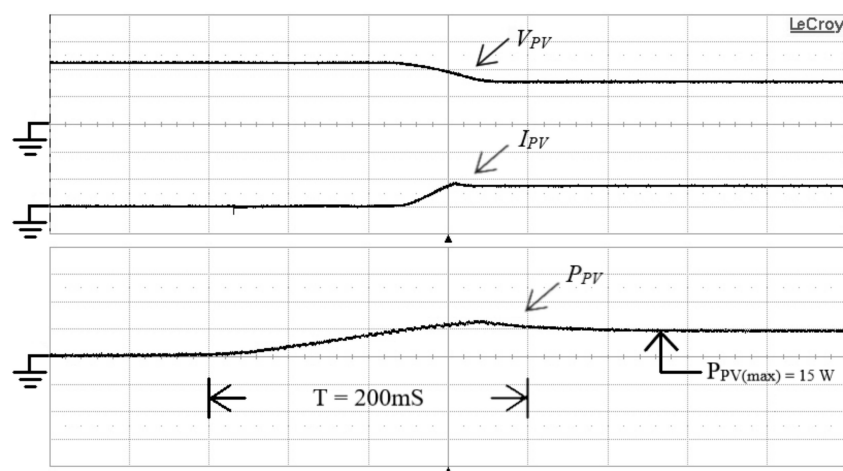


Figure 16. Photo of the proposed hybrid converter prototype.

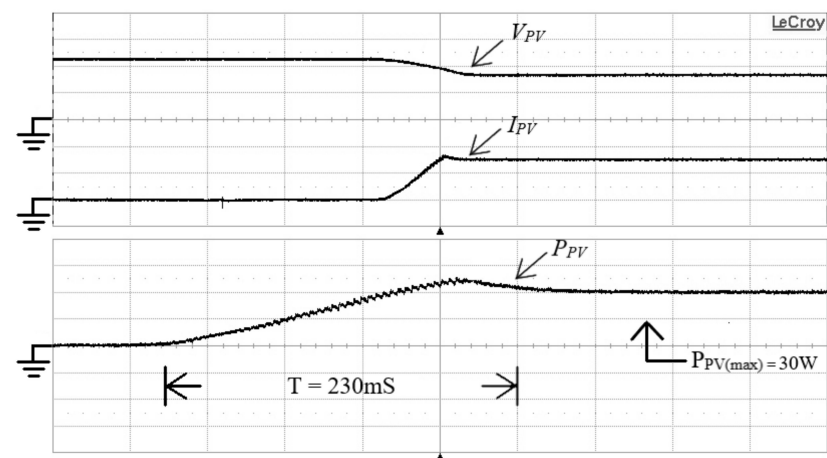
Table 6. Layout area comparison between the propose hybrid converter and the conventional counterpart converter.

Component	The Conventional Counterpart Converter Shown in Figure 4			The Proposed Hybrid Converter Shown in Figure 5		
	Symbol	Dimension (Length × Width)	Circuit Layout Dimension (Length × Width)	Symbol (Length × Width)	Dimension (Length × Width)	Circuit Layout Dimension (Length × Width)
Switches (heat sink dimension Length × width = 15 mm × 10 mm)	Switch M_1 with heat sink	10 mm × 5 mm $S_{M1} = 50 \text{ mm}^2$	25 mm × 20 mm $S_{PM1} = 500 \text{ mm}^2$	Switch M_1 with heat sink	10 mm × 5 mm $S_{M1} = 50 \text{ mm}^2$	25 mm × 20 mm $S_{PM1} = 500 \text{ mm}^2$
	Switch M_2 with heat sink	10 mm × 5 mm $S_{M2} = 50 \text{ mm}^2$	25 mm × 20 mm $S_{PM2} = 500 \text{ mm}^2$	Switch M_2 with heat sink	10 mm × 5 mm $S_{M2} = 50 \text{ mm}^2$	25 mm × 20 mm $S_{PM2} = 500 \text{ mm}^2$
	Switch M_3 with heat sink	10 mm × 5 mm $S_{M3} = 50 \text{ mm}^2$	25 mm × 20 mm $S_{PM3} = 500 \text{ mm}^2$	Switch S_1 without heat sink	10 mm × 5 mm $S_{S1} = 50 \text{ mm}^2$	20 mm × 15 mm $S_{PS1} = 300 \text{ mm}^2$
Magnetics (EE-33 core)	Inductor L_1	35 mm × 35 mm $S_{L1} = 1225 \text{ mm}^2$	45 mm × 45 mm $S_{PL1} = 2025 \text{ mm}^2$	Transformer T_r	35 mm × 35 mm $S_{Tr} = 1225 \text{ mm}^2$	45 mm × 45 mm $S_{PTr} = 2025 \text{ mm}^2$
	Transformer T_r	35 mm × 35 mm $S_{Tr} = 1225 \text{ mm}^2$	45 mm × 45 mm $S_{PTr} = 2025 \text{ mm}^2$			
Diodes	Diode D_1 with heat sink	10 mm × 5 mm $S_{D1} = 50 \text{ mm}^2$	25 mm × 20 mm $S_{PD1} = 500 \text{ mm}^2$	Diode D_1 with heat sink	10 mm × 5 mm $S_{D1} = 50 \text{ mm}^2$	25 mm × 20 mm $S_{PD1} = 500 \text{ mm}^2$
	Diode D_2 with heat sink	10 mm × 5 mm $S_{D2} = 50 \text{ mm}^2$	25 mm × 20 mm $S_{PD2} = 500 \text{ mm}^2$			
	Diode D_B with heat sink	10 mm × 5 mm $S_{DB} = 50 \text{ mm}^2$	25 mm × 20 mm $S_{PDB} = 500 \text{ mm}^2$	Diode D_B with heat sink	10 mm × 5 mm $S_{DB} = 50 \text{ mm}^2$	25 mm × 20 mm $S_{PDB} = 500 \text{ mm}^2$
others	Fuse, connector, Driving circuit and filter	$S_{PT} > 1675 \text{ mm}^2$		Fuse, connector, Driving circuit and filter	$S_{PT} = 1675 \text{ mm}^2$	
Total circuit layout area S_{TA}		$S_{TA} > 8725 \text{ mm}^2$ (=9000 mm^2)			$S_{TA} = 6000 \text{ mm}^2$	



(V_{PV} : 10 V/div, I_{PV} : 1 A/div, P_{PV} : 15 W/div, time: 50 ms/div)

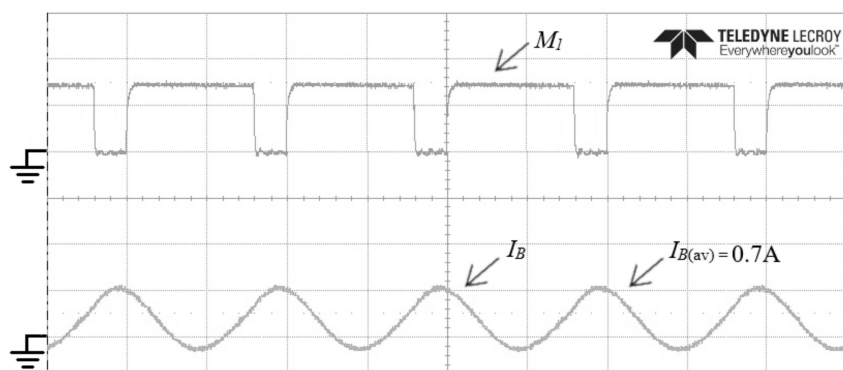
(a)



(V_{PV} : 10 V/div, I_{PV} : 1 A/div, P_{PV} : 15 W/div, time: 50 ms/div)

(b)

Figure 17. Measured voltage V_{PV} , current I_{PV} and power P_{PV} of solar power under maximum power point tracking (MPPT): (a) $P_{PV(max)} = 15 \text{ W}$, and (b) $P_{PV(max)} = 30 \text{ W}$.



(M_I : 10 V/div, I_B : 2 A/div, time: 5 $\mu\text{s}/\text{div}$)

(a)

Figure 18. Cont.

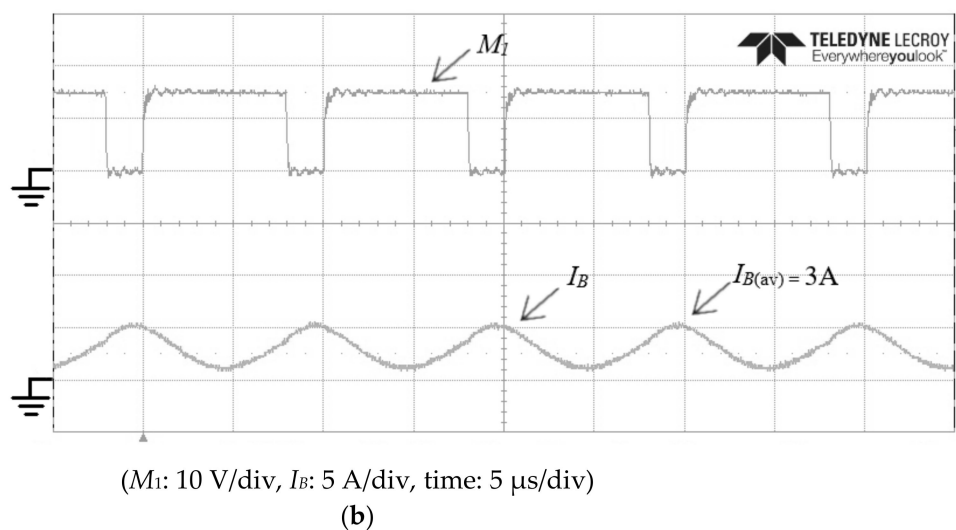


Figure 18. Measured gate voltage M_1 and charging current I_B of the proposed hybrid converter operated in the charging mode: (a) under the average charging current $I_{B(av)} = 0.7$ A, and (b) under $I_{B(av)} = 3$ A.

Since the proposed hybrid converter was operated in the discharging mode, switches M_1 and M_2 were operated with ZVS at turn-on transition. When the proposed hybrid converter was operated in the discharging mode, measured switch voltages V_{M1} , V_{M2} and currents I_{M1} , I_{M2} waveforms of the proposed hybrid converter are shown in Figure 19. Figure 19a,b show those waveforms under 10% of full-load condition, while Figure 20a,b illustrate those waveforms under 15% of full-load condition. From Figures 19 and 20, it can be found that switch M_1 and M_2 were operated with ZVS at turn-on transition under 10–15% of full-load condition, simultaneously. Figure 21 illustrates measured output voltage V_o and output current I_o under step-load change between 0% of full-load and 100% of full-load conditions, from which it can be obtained that the voltage regulation of output voltage V_o was limited within $\pm 1\%$.

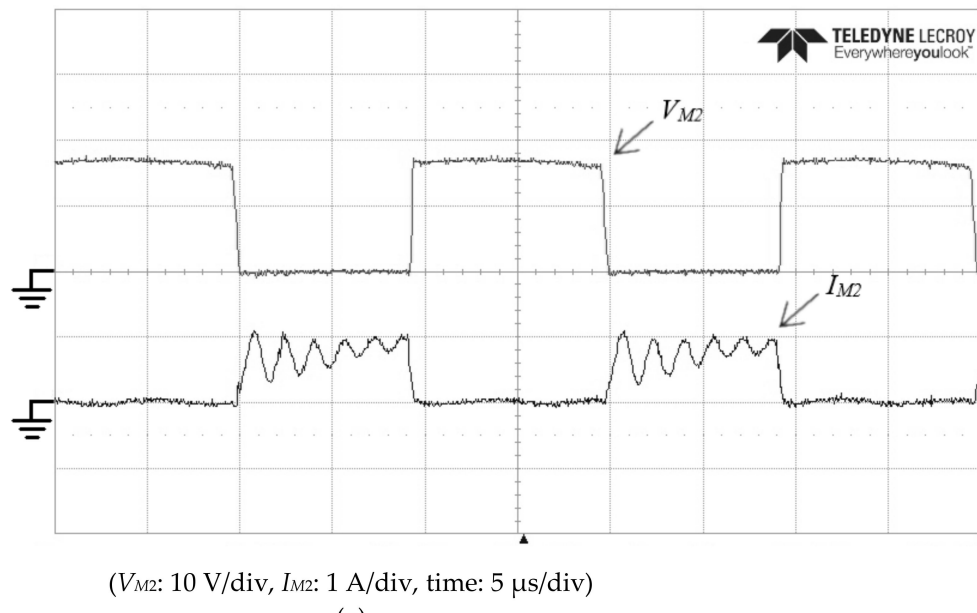


Figure 19. Cont.

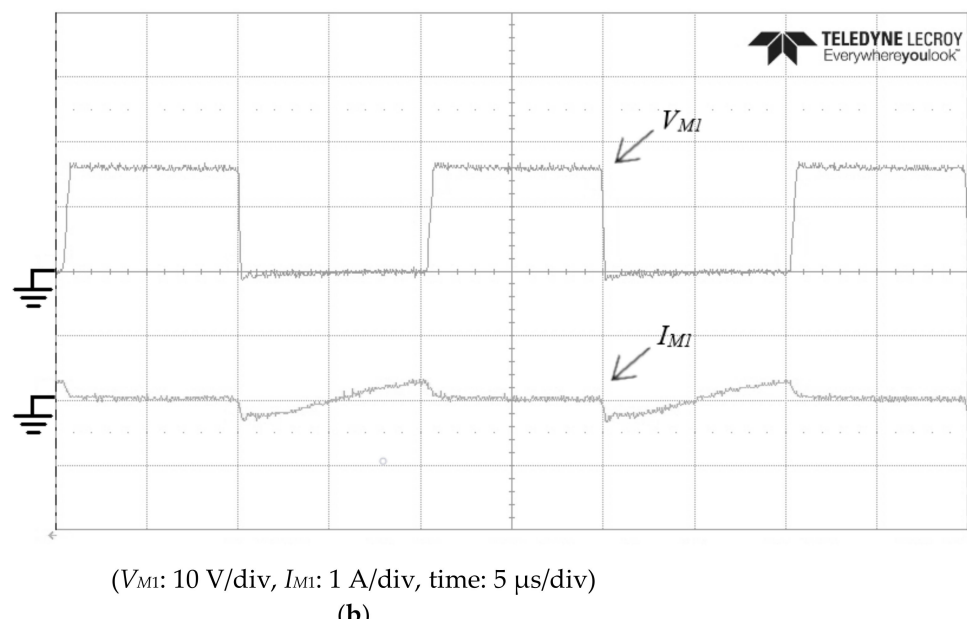


Figure 19. Measured voltage V_{M1} , V_{M2} and currents I_{M1} , I_{M2} waveforms of the proposed hybrid converter operated in the discharging mode: (a) voltage V_{M2} and current I_{M2} , and (b) voltage V_{M1} and current I_{M1} under 10% of full-load condition.

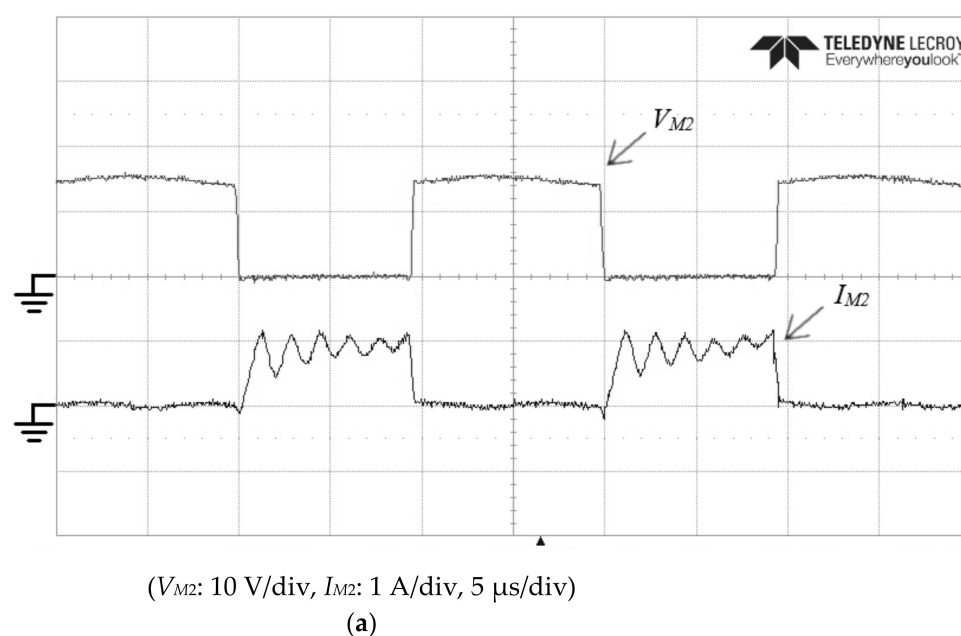


Figure 20. Cont.

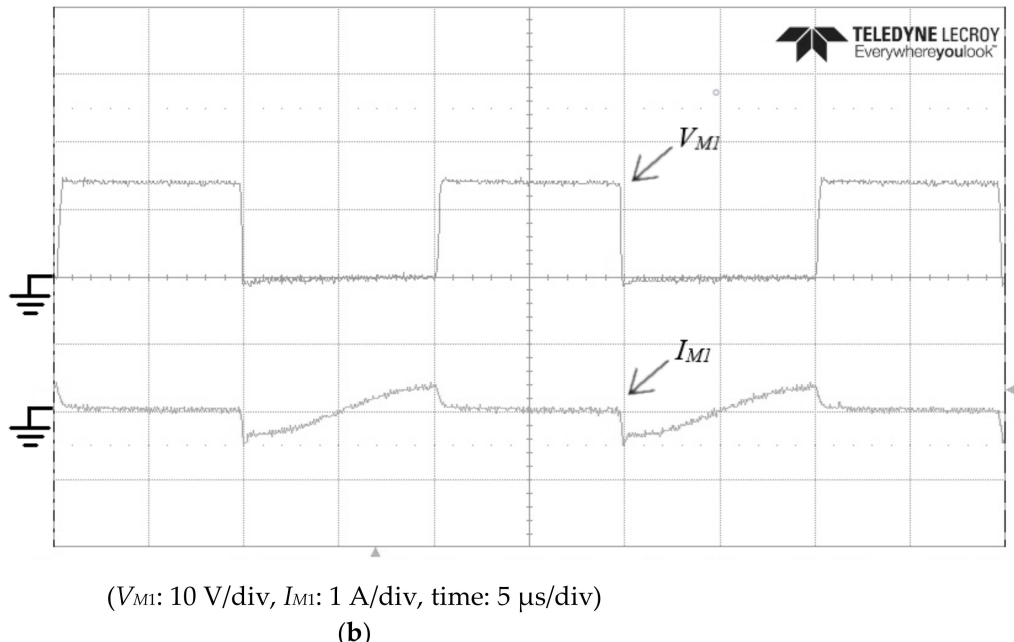


Figure 20. Measured voltage V_{M1} , V_{M2} and currents I_{M1} , I_{M2} of the proposed hybrid converter operated in the discharging mode: (a) voltage V_{M2} and current I_{M2} , and (b) voltage V_{M1} and current I_{M1} under 15% of full-load condition.

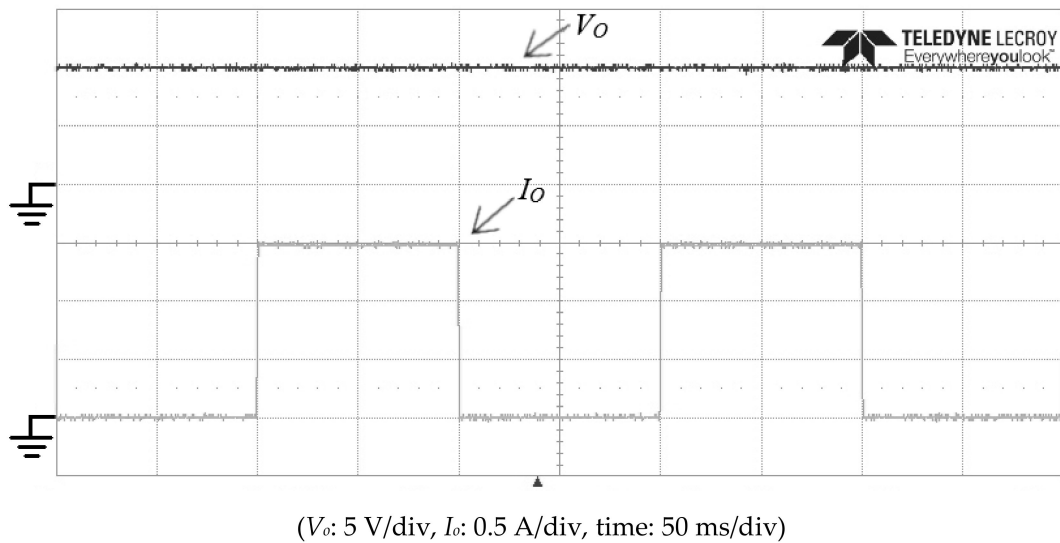


Figure 21. Measured output voltage V_o and output currents I_o waveforms of the proposed hybrid converter operated in the discharging mode under step-load changes between 0% and 100% of full-load condition.

Comparison of conversion efficiency between flyback converter with hard-switching circuit and with the proposed active clamp circuit from light load to heavy load is shown in Figure 22, illustrating that the efficiency of the proposed converter is higher than that of hard-switching one. Its efficiency was 85% under full-load condition. According to component selection of the proposed hybrid converter, key component parameters are listed in Table 7. Power loss analysis of the proposed hybrid converter under full-load condition is illustrated in Table 8. Total power losses included switch, diode, transformer and driving circuit in the proposed hybrid one. The driving circuit loss was measured by oscillator and voltage V_{cc} is 12 V and current I_{cc} was 17.7 mA. The driving circuit loss P_{DC} was 0.21 W. Since switches M_1 and M_2 were operated with ZVS at turn-on transition,

their switching loss only considered switching loss at turn-off transition. According to the maximum operational current and voltage of switch, diode and transformer in the proposed hybrid converter, losses of each component are listed in Table 8. Switch S_1 was one time in the turn-on or turn-off state during a day. Its loss was only conduction loss. According to (33) and Table 4, maximum flux density B_m can be determined and its value was 200 mT. Figure 23 shows the core loss curves of transformer T_r manufactured by PC95 material of TDK. When $B_m = 200$ mT, core coefficient C_p is equal to 110 mW/cm³. Effective core volume V_e of transformer T_r was equal to 8.03 cm³. The core loss could be determined and its value P_{cpTr} = 0.88 W. In addition, copper loss P_{cpTr} could be obtained by (35). Since $I_{D1(rms)} = I_{S1(rms)} = 2.55$ A, $I_{Lm2(rms)} = 6.5$ A, $R_{dc1}l_{m1} = 0.027$ Ω and $R_{dc2}l_{m2} = 0.062$ Ω, copper loss P_{cpTr} equaled 1.54 W. The conversion efficiency of the proposed hybrid converter operated in the discharging mode was 86.6% under full-load condition. The practical conversion was 85%. The stray loss of the proposed hybrid converter was 1.6%.

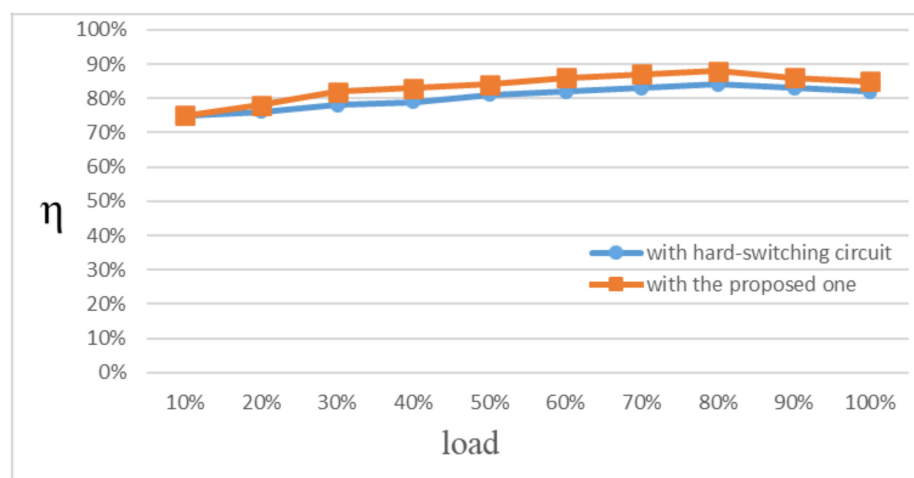


Figure 22. Comparison conversion efficiency between the conventional hard-switching flyback converter and the proposed one from light load to heavy load for operating in the discharging mode.

Table 7. Key component parameters of the proposed hybrid converter.

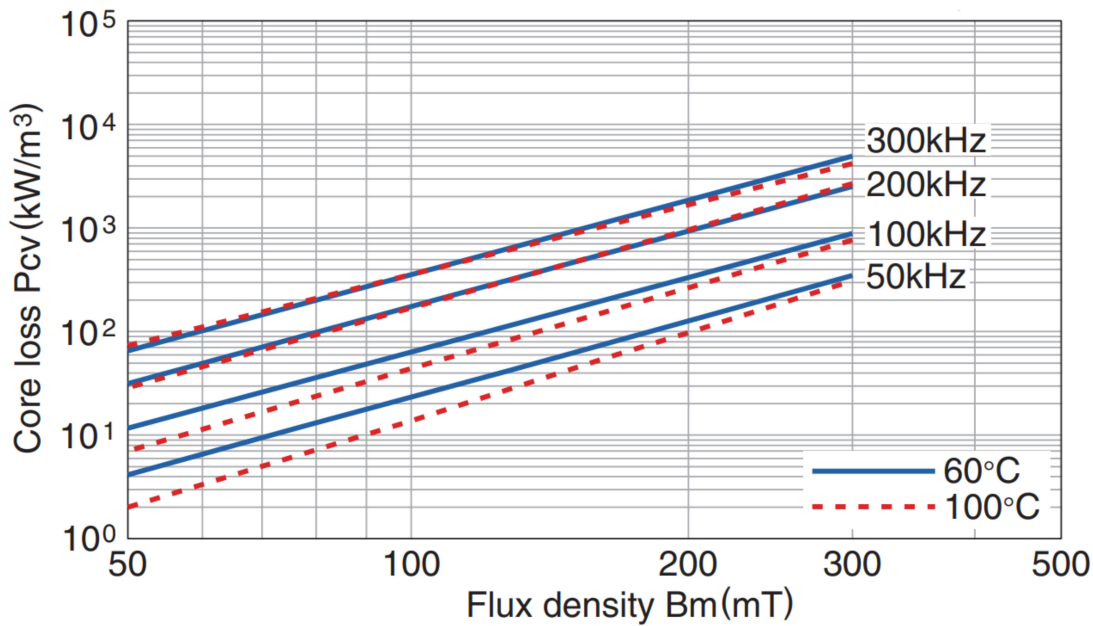
Component	Part Number	Voltage/Current Ratings Or Formula	Features		
			Symbol	Parameter	Values
Transformer T_r	TDK EE-33 (PC95 material)	$M_{1,2}$ S_1 A_{ow2918} D_1 $STPS10L60D$ $I_{pk} = \frac{N I_{o(max)}}{1 - D_{12(max)}} + \frac{\Delta I_{LM2}}{2}$ (A) $\mu_0: 4\pi \times 10^{-7}(\text{H/m})$ I_{PK} : maximum inductor current of primary winding (A) $I_{D(max)}$: output maximum current (A) $D_{12(max)}$: maximum duty cycle of switch M_2 ΔI_{Lm2} : variation of current I_{Lm2} (A) N : turns of primary winding A_e : Effective core volume (m^2)	$R_{DS(on)}$	Drain-source On resistance	<7 mΩ
			t_{on}	Turn-on transition time	41 nS
			t_{off}	Turn-off transition time	54 nS
			V_F	Forward drop voltage	0.56 V
			μ_r	permeability	3300
			A_e	Effective cross-sectional area	119 mm ²
			l_e	Effective magnetic Path length	67.5 mm
			V_e	Effective core volume	8030 mm ³
			l_g	Air gap length	0.8 mm
			l_{n1}	Approximate mean length of turn in primary winding	64 mm
			l_{n2}	Approximate mean length of turn in secondary winding	72 mm
			AWG#18	Wire gauges of primary and secondary windings	Diameter 1.0 mm
				R_{dc} : resistance	21.4 mΩ/m

Table 7. Cont.

Component	Part Number	Voltage/Current Ratings Or Formula	Features		
			Symbol	Parameter	Values
			N_1	turn of primary winding	20 Turns
			N_2	turn of secondary winding	40 Turns
			$R_{dc1}l_{m1}$	Resistance of primary winding	0.027 Ω
			$R_{dc2}l_{m2}$	Resistance of secondary winding	0.062 Ω

Table 8. Power loss analysis of the proposed hybrid converter under $V_B = 12$ V and output maximum current $I_{o(max)} = 2$ A.

Component	The Proposed Hybrid Converter		Total Power Losses of Each Component
	Symbol	Power Loss	
Driving circuit	P_{DC}	$P_{DC} = I_{cc} \times V_{cc}$ $= 17.7 \times 12 \times 10^{-3} = 0.21$ w	$P_{DC} = 0.21$ w
Switch M_1	Switching loss P_{CM1}	$P_{CM1} = 0.15$ w	$P_{CDM1} = 0.24$ w
	Conduction loss P_{DM1}	$P_{DM1} = 0.09$ w	
Switch M_2	Switching loss P_{CM2}	$P_{CM2} = 0.15$ w	$P_{CDM2} = 0.26$ w
	Conduction loss P_{DM2}	$P_{DM2} = 0.11$ w	
Switch S_1	Conduction loss P_{DS1}	$P_{DS1} = 0.05$ w	$P_{DS1} = 0.05$ w
Diodes D_1	Forward drop loss P_{D1}	$P_{D1} = 1.43$ w	$P_{D1} = 1.43$ w
Transformer T_r	Core loss P_{cTr}	$P_{cTr} = 0.88$ w	$P_{cpTr} = 2.45$ w
	Copper loss P_{cpTr}	$P_{cpTr} = 1.54$ w	
Efficiency		86.6%	

**Figure 23.** Core loss (mW/cm^3) curves of transformer T_r manufactured by PC95 material of TDK.

6. Conclusions

The proposed hybrid converter is consisted of buck-boost converter and active flyback converter to implement battery charger and discharger. Circuit derivation of the proposed

hybrid converter is presented in this paper for decreasing component count. Moreover, operational principle, steady-state analysis, design and power loss analysis of the proposed hybrid converter have been described in detail. As compared with the conventional counterparts with hard-switching circuit, the proposed one can increase conversion efficiency of 4% and achieve efficiency of 85% under full load condition when the proposed one is operated in the discharging mode. In addition, cost and power density comparison between the proposed hybrid converter and the conventional counterpart converter, the proposed hybrid one can reduce cost of 19–22.7% and power density of the proposed one can increase about 1.5 times. An experimental prototype has been implemented for lithium battery of 12 V/3.2 Ah and for LED lighting of 10 V/2 A. It can verify the feasibility of the proposed hybrid converter. It is suitable for solar power applications.

Author Contributions: Conceptualization, methodology, and writing—original draft preparation, S.-Y.T.; writing—review and editing, J.-H.F. All authors have read and agreed to the published version of the manuscript.

Funding: This research was funded by Ministry of Science and Technology (MOST) in Taiwan grant number MOST 109-2622-E-182-003-cc3.

Conflicts of Interest: The authors declare no conflict of interest.

References

1. Alghaythi, M.L.; O'Connell, R.M.; Islam, N.E.; Khan, M.M.S.; Guerrero, J.M. A High Step-Up Interleaved DC-DC Converter with Voltage Multiplier and Coupled Inductors for Renewable Energy Systems. *IEEE Trans. Ind. Electron.* **2020**, *8*, 123165–123174.
2. Sahli, A.; Krim, F.; Laiband, A.; Alam, M.S.; Talbi, B. Energy management and power quality enhancement in grid-tied single-phase PV system using modified PUC converter. *IET Renew. Power Gener.* **2019**, *13*, 2512–2521. [[CrossRef](#)]
3. Castro, I.; Vazquez, A.; Aller, D.G.; Arias, M.; Lamar, D.G.; Sebastian, J. On Supplying LEDs from Very Low DC Voltages with High-Frequency AC-LED Drivers. *IEEE Trans. Power Electron.* **2018**, *34*, 5711–5719. [[CrossRef](#)]
4. Wang, Y.; Hu, X.; Guan, Y.; Xu, D. A Single-Stage LED Driver Based on Half-Bridge CLCL Resonant Converter and Buck-Boost Circuit. *IEEE Trans. Ind. Appl.* **2019**, *7*, 196–208. [[CrossRef](#)]
5. Tsou, M.C.; Kuo, M.T. Optimal Combination Design of a Light Emitting Diode Matrix Applicable to a Single-Stage Flyback Driver. *Energies* **2020**, *13*, 5209. [[CrossRef](#)]
6. Alonso, J.M.; Vina, J.; Vaquero, D.G.; Martinez, G.; Osorio, R. Analysis and design of the integrated double buck-boost converter as a high-power-factor driver for power-LED lamps. *IEEE Trans. Ind. Electron.* **2012**, *59*, 1689–1697. [[CrossRef](#)]
7. Chen, Y.S.; Liang, T.J.; Chen, K.H.; Juang, J.N. Study and implementation of high frequency pulse LED driver with self-oscillating circuit. In Proceedings of the 2011 IEEE International Symposium of Circuits and Systems (ISCAS), Rio de Janeiro, Brazil, 15–18 May 2011; pp. 498–501.
8. Wang, Y.; Zhang, S.; Alonso, J.M.; Liu, X.; Xu, D. A high efficiency driver for high-brightness white LED lamp. In Proceedings of the IEEE TENCON Conference, Jeju Island, Korea, 28–31 October 2018.
9. Lee, S.W.; Do, H.L. A Single-Switch AC-DC LED Driver Based on a Boost-Flyback PFC Converter with Lossless Snubber. *IEEE Trans. Power Electron.* **2016**, *32*, 1375–1384. [[CrossRef](#)]
10. Cheng, C.A.; Chang, C.H.; Chung, T.Y.; Yang, L. Design and Implementation of a Single-Stage Driver for Supplying an LED Street-Lighting Module With Power Factor Corrections. *IEEE Trans. Power Electron.* **2015**, *30*, 956–966. [[CrossRef](#)]
11. Chen, X.; Pise, A.A.; Elmes, J.; Bataresh, I. Ultra-Highly Efficient Low-Power Bidirectional Cascaded Buck-Boost Converter for Portable PV-Battery-Devices Applications. *IEEE Trans. Ind. Appl.* **2019**, *55*, 3989–4000. [[CrossRef](#)]
12. Kim, K.D.; Lee, H.M.; Hong, S.W.; Cho, G.H. A Non-inverting Buck-Boost Converter with State-Based Current Control for Li-ion Battery Management in Mobile Applications. *IEEE Trans. Ind. Electron.* **2019**, *66*, 9623–9627. [[CrossRef](#)]
13. Pouladi, F.; Farzanehfard, H.; Adib, E. Battery Operated Soft Switching Resonant Buck-Boost LED Driver with Single Magnetic Element. *IEEE Trans. Power Electron.* **2019**, *34*, 2704–2711. [[CrossRef](#)]
14. Rezaei, M.A.; Lee, K.J.; Huang, A.Q. A High-Efficiency Flyback Micro-inverter with a New Adaptive Snubber for Photovoltaic Applications. *IEEE Int. Power Electron.* **2016**, *31*, 318–327. [[CrossRef](#)]
15. Kwon, M.; Kwon, B.H. High step-up active-clamp converter with input-current doubler and output-voltage doubler for fuel cell power systems. *IEEE Trans. Power Electron.* **2009**, *24*, 108–115. [[CrossRef](#)]
16. Silva, M.P.; Perez, D.S.; Benitez, O.M.R.; Valdes, L.G.V.; Sanchez, A.C.; Aldaco, S.E.D.L.; Garcia, C.C.; Benitez, Y.I.S.; Ponce, R.E.L.; Tapia, J.A.A. Flyback Converter for Solid-State Lighting Applications with Partial Energy Processing. *Energies* **2021**, *10*, 60.
17. Tseng, S.Y.; Hauang, P.J.; Wu, D.H. Power Factor Corrector with Bridgeless Flyback Converter for DC Loads Applications. *Energies* **2018**, *11*, 3096. [[CrossRef](#)]